Effect of fibre concentration on the mechanical properties of welded reinforced polypropylene

E. Mofakhami [a,b,c], L. Gervat [a], B. Fayolle [b], G. Miquelard-Garnier [b], C. Ovalle [c,*], L. Laiarinandrasana [c]

[a] Renault Technocentre, DEA-TC, 78084 Guyancourt, France
[b] Laboratoire PIMM, Arts et Metiers Institute of Technology, CNRS, Cnam, HESAM University, 75013 Paris, France
[c] Mines Paris, PSL University, Centre for Material Sciences (MAT), UMR7633 CNRS, 91003 Evry, France

ARTICLE INFO

Keywords:
Vibration welding
Thermoplastic composites
Short glass fibres
X-ray microtomography
Mechanical properties

ABSTRACT

The effects of fibre concentration on the mechanical response of welded glass-fibre-reinforced polypropylene (GF-PP) were studied in-depth. Experimental observations during tensile tests of unwelded and welded GF-PP have shown a weld ratio reduction – ratio between the strength of the welded material and that of the bulk material – as high as 60%. For all conditions studied, no significant change in the polymer matrix was observed. Increasing the fibre content on the welded material was additionally associated with a decrease in the stress at break and the strain at the maximum stress, respectively 68 and 84% for 50 wt% GF-PP. The DIC technique was used to retrieve the local response in the welded zone, showing local strain as high as 19.5 times the macroscopic strain. Using X-ray microtomography, the strain magnification could be explained by the significant increase of the fibre density at the welded zone. It was also shown that at least 2/3 of the fibres were orientated within the weld plane limiting the transverse strain, favouring void nucleation and embrittlement of the material. As a consequence, the rupture can be explained by the amplification of the strain linked with the fibre concentration and orientation of the welded material.

1. Introduction

To facilitate the design of complex parts but also to reduce the total weight and lower the energy consumption, composites are replacing metals in many industrial sectors, such as automotive or transport in general [1]. A common strategy consists of injection moulding short-glass-fibre-reinforced thermoplastics such as polyamide (SGF/PA) or a cheaper polypropylene (SGF/PP). Because in some cases (hollow parts and complex geometries), it is not possible to inject the whole piece at once [2], welding is then used to join the two separately injected halves.

Several welding methods can be used in the industry to join plastic or metal parts, but they commonly rely on friction at the interfaces, a process that has been termed friction stir welding [3]. Friction can be coupled with vibration or ultrasonic vibration of the parts to join [4–6]. This method, historically developed for metal parts, has been adapted quite recently to polymer thermoplastics, thermosets and composites [7–10].

Still, vibration welding alone is generally sufficient to weld polymer parts and vibration welding is then the common method used in the industry for reinforced semi-crystalline thermoplastics such as SGF/PP and SGF/PA. In the case of high performance thermoplastics composites (for example carbon fibres reinforced polyphenylsulfide), ultrasonic vibration can be envisioned [11].

The vibration welding process has been described in detail by Stokes [12,13] and the different steps are summarised in our previous study [14]. Briefly, this operation involves applying a pressure at the interface between the two parts, then horizontally rubbing one part against the other fixed one, at a given frequency and amplitude. The friction locally melts the polymer at the interface, allowing to join the parts. When a preset meltdown depth or time is reached, vibration is stopped and pressure is maintained during cooling until the joint is obtained. The main point is that, since the cooling profile and polymer flows are not the same between welding and injection operations, the microstructure, for example, the crystalline morphology [15] in the heat-affected zone, differs from that of the bulk material [16].

However, in the case of reinforced thermoplastics, an important fundamental question is understanding the role of fibres in the loss of failure characteristics of welded parts, compared with their unwelded counterparts. The weld ratio, defined as the ratio of tensile strength for welded and unwelded materials, can reach 0.97 for unfilled polymers

* Corresponding author.
E-mail address: cristian.ovalle_rodas@minesparis.psl.eu (C. Ovalle).

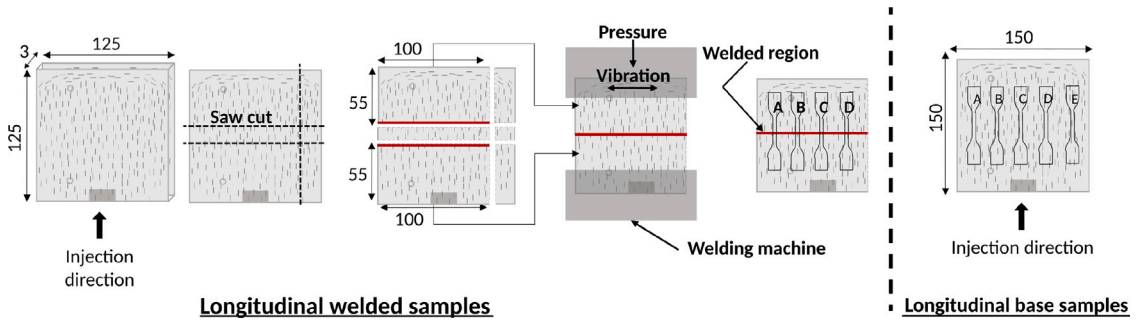

Fig. 1. Sketch of the samples preparation.

but decreases significantly with the addition of short glass fibres in the polymer matrix [17]. Increasing the amount of fibres in the composite actually leads to a monotonic decrease of the weld ratio [17,18], from 0.97 with no fibre to 0.39 with 45 wt% of glass fibres in the composite. Moreover, the maximum strength that can be reached for the joint is only 10% higher than the one of the pure matrix, and is achieved at low amounts of fibres (in the 15–25 wt% range). Indeed, the mechanisms explaining this drastic loss of weld ratio value for short-fibre composites during welding are not fully understood [19] but the admitted qualitative reason is that fibres are reoriented towards the vibration and the squeeze flows directions occurring during welding, leaving a small amount of fibres in the joining direction in the welded zone [18,20]. This reorientation is consequently unfavourable because it is mainly in the direction perpendicular to the direction of the tensile load. However, some defects induced by the processing such as residual porosity or locally degraded polymer can also contribute to the loss of mechanical properties. This point has especially been investigated in the case of SLS 3D printing [21]. Anyhow, assuming that fibre reorientation is the major cause of mechanical loss, a few articles have attempted to develop robust methodologies to quantify fibre reorientation [14,19,22–24] during welding, the impact of fibre content on this reorientation has not yet been studied in detail.

In this work we aimed at a better understanding of why increasing the content of glass fibres leads to a decrease in the weld strength. To do so, we studied 4 amounts of glass fibres (0, 20, 35, 50 wt%) in welded polypropylene injected plates with fibres, initially, mainly oriented in the loading direction. To assess the relationships between microstructure and mechanical properties, different scales were studied. First, crystallinity and molar mass changes of the matrix were assessed since these changes could be associated with possible thermal degradation mechanisms induced by the processing [25]. Second, fibre reorganisation (both reorientation and agglomeration) and void nucleation were quantitatively probed using high-resolution synchrotron-based X-ray microtomography [26], following the protocols optimised in our previous study on the links between welding parameters and mechanical properties of welded PA6 [14]. Linking these observations to tensile tests, digital image correlation and the tomography of interrupted tensile tests close to the breaking point, a scenario of rupture is proposed.

2. Materials & methods

2.1. Materials

Polypropylene (PP) pellets with various amounts of short glass fibres (SGF) (0, 20, 35 and 50 wt%) were kindly provided by Sumika Polymer Compounds®. In the following, they will be called "base materials" and noted, respectively, as PP-GF0, PP-GF20, PP-GF35 and PP-GF50. They are non-commercial products designed for the study: the same matrix and additives such as carbon black and stabilisers were used for all formulations after being optimised for the 35 wt% concentration, which is the typical concentration for commercial use. SGFs have a mean diameter of 13 μm, common for PP reinforcement.

The pellets were injected on an injection moulding machine DK CODIM®175/410 to form plates with dimensions of 125 × 125 × 3 mm. The injection parameters were set as follows for all samples: mould temperature was constant at 60 °C, the temperature was 240 °C at the entry point, maintenance time was 30 s and cooling lasted 80 s. The only parameter depending on the amount of SGF was the injection pressure, which varied between 500 and 700 bars.

2.2. Welding

Prior to welding, the samples were cut using a band saw, to obtain samples well-dimensioned for the vibration welding machine, but also to work with longitudinally welded samples, *i.e.* with fibres initially mostly oriented perpendicular to the weld (see Fig. 1).

The "longitudinal" configuration sketched in Fig. 1, though not typical for industrial pieces, has been chosen to enhance the effect of welding on the resulting mechanical properties (see [14]) when compared with non-welded samples. It will indeed exhibit higher initial stiffnesses or strengths and hence a bigger drop after welding, than the more usual "transversely" welded configuration used in most industrial parts.

Plates were welded using a Branson vibration welding machine at Branson facilities (Dietzenbach, Germany), with the help of Novarest. The frequency was set at 240 Hz, the amplitude was fixed at 1.6 mm and the meltdown depth equal to 1.5 mm. Note that the typical roughness of the cut parts is on the order of a few μm, negligible when compared to the meltdown depth. The welding pressure was set at 1.5 MPa. Two kinds of samples were produced:

- Base (non welded) material samples: PP-GF0, PP-GF20, PP-GF35 and PP-GF50;
- Welded material samples constituted of:
  - Weld material at mid-height: Weld-GF0, Weld-GF20, Weld-GF35 and Weld-GF50;
  - Base material surrounding the Weld material.

Base material is present in both samples whereas Weld material is just located at mid-height of the welded material sample.

2.3. Size exclusion chromatography

Weight average molecular weight M_w, number average molecular weight M_n and dispersity defined as $D_M = M_w/M_n$ were obtained from size exclusion chromatography (SEC) on a high-temperature Agilent Series PL-GPC 220 apparatus (Agilent Technologies, Santa Clara, USA) equipped with two columns PLGel Olexis and a refractive index detector, following the protocol described in [27]. Briefly, about 10 mg of pellets, injected and welded plates were dissolved in a few mL of 1,2,4-trichlorobenzene (Merck Sigma Aldrich) containing 0,3% 2,6-di-tert-butyl-4-methylphenol (Merck Sigma Aldrich) at 135 °C during

20 min. 200 μL of the solutions were injected with a flow rate of 1 mL/min. The samples containing glass fibres were filtered prior to injection.

2.4. Crystallinity measurement

Differential Scanning Calorimetry (DSC) measurements were performed on a Q1000 from TA Instruments calibrated with Indium. Several layers with a thickness of 50 μm were taken from the plates (in bulk and welded regions) using a LEICA microtome and stacked into non-hermetic aluminium pans to reach a total mass between 5 and 10 mg. The DSC analyses were performed under a nitrogen flow of 50 mL/min by applying a temperature sweep from −30 °C to 300 °C at a rate of 10 °C/min. Two measurements were performed for each condition to ensure reproducibility. Crystallinity was determined using the following relation:

$$\chi_c = \frac{\Delta H_m}{w \times \Delta H_{m0}} \tag{1}$$

with w the mass fraction of polymer in the composite. It was verified with a thermogravimetric analyser from TA Instruments TGA Q50, using the same samples as in DSC, that the value given by the supplier was consistent. Values in-between 35.2 and 36.2 wt% were for example obtained for PP-GF35. This is in good agreement but since these values also include other additives such as carbon black, the values given by the supplier will be used in the calculations. Finally, in Eq. (1), ΔH_m is the measured melting enthalpy, and the melting enthalpy for a 100% crystalline PP ΔH_{m0} is equal to 207 J/g [28]. The measured melting enthalpy was obtained by integrating the crystal's fusion peak area of the heat flow curve from 130 °C to the end of the fusion peak.

2.5. Tensile tests

Tensile tests were performed at 10^{-4} s^{-1} on ISO527-5A samples with a thickness of 3 mm to investigate the material response under quasi-static loading. Six dumbbell-shaped samples were machined from both base and welded plates, as illustrated in Fig. 1.

Tensile tests were performed at room temperature on an Instron machine model 5966 equipped with a 10 kN load cell and a video-extensometer to follow the displacement ΔL between two white dots which were drawn on each part of the weld with a spacing distance $L_0 = 1$ cm. The engineering strain ε and stress σ were obtained using, respectively, the relations $\varepsilon = \Delta L/L_0$, and $\sigma = F/S_0$ with F the applied load and S_0 the initial section area of the sample (which was measured for each sample before the test and approximately equal to 12 mm^2). For base samples, non-welded ones, L_0 was equal to the gauge length suggested in the ISO527-5A standard. The gauge length is then larger than the spacing distance in welded samples; however, the engineering strain does not change significantly because no necking appeared during the tests.

2.6. Digital image correlation (DIC)

The tensile tests were followed by digital image correlation, VicSnap®software, and synchronised with the load and the cross head displacement from the testing machine. The dumbbell-shaped samples were painted in white and then covered with a black speckle by using an air-brush gun. The images were analysed with the Vic-2D®software. The subset size was optimised as a square image of dimensions 62 × 62 pixels (280 × 280 μm). Two engineering strains were issued from the software:

- the longitudinal strain noted as $\delta l/l_0$;
- the transverse strain through the width of the specimen named as $\delta w/w_0$.

These latter strains were also synchronised with the data from the testing machine at two "local" volumes of interest (VOI):

- the weld VOI located at mid-height;
- the base material VOI above the weld one.

2.7. High-resolution synchrotron-based X-ray microtomography

X-ray microtomography was performed at SOLEIL Synchrotron on the Anatomix beamline [29] following the protocol detailed in [14]. Briefly, the beam energy was set to 16 keV and the voxel edge size was 0.65 μm. A total of 2000 projections per scan were recorded during a 180° rotation. 50 pictures taken before and after sample acquisition were used for the reconstruction of scanned volumes with a Paganin filter. Three scans were performed and joined together to analyse the entire sample thickness (3 mm).

Fig. 2 shows a representative image of a slice extracted from 3D data sets for the PP-GF35 sample. A skin-shell-core effect [23], induced by the injection moulding process, is visible along the thickness. The red lines indicate the position of the welded region and weld flash is visible at both extremities of the plates. Fibre reorientation and void presence (darker regions) can also be observed. In the bottom part of the figure, the welded region is shown for samples with various SGF contents.

From these data, information can be extracted. Fibre reorientation is characterised in and out the welded zone with the Xfibre®extension in Avizo®Software [30] on 20 subvolumes of dimensions 500 μm × 50 μm × 500 μm centred at 750 μm from the edge throughout the weld, as illustrated in Fig. 2.

The orientation angles (θ and ϕ) of each fibre in spherical coordinates are obtained and used to determine the diagonal terms of fibre orientation tensors (a_{xx}, a_{yy}, a_{zz}) [31], as shown in Eqs. (2)–(4):

$$a_{xx} = \langle \sin^2\theta \times \cos^2\phi \rangle \tag{2}$$

$$a_{yy} = \langle \sin^2\theta \times \sin^2\phi \rangle \tag{3}$$

$$a_{zz} = \langle \cos^2\theta \rangle \tag{4}$$

The heights of the welded regions are noted in Fig. 2. It can be noticed that the higher the fibre content, the larger the height of the welded zone. It seems to indicate that the work of the applied pressure is less efficient for higher fibre contents.

The fibre volume fraction was obtained in each subvolume with an image analysis performed using the Fiji®software, consisting in thresholding the pictures. The 3D-visualisation was performed using a Pymicro python open source package [32]. A similar protocol was applied to determine the void volume fraction on a chosen representative set to 2400 ~ 2800 μm × 1330 μm × 325 μm.

3. Results and discussion

3.1. Mechanical properties

3.1.1. Base versus welded materials

As aforementioned, the weld ratio [17] is defined as the strength (maximum stress) of the welded material divided by that of the base material.

$$W_c^{\sigma_{max}} = \frac{\sigma_{max}^W}{\sigma_{max}^B} \tag{5}$$

where superscripts B and W stand for "Base" and "Welded" materials, respectively.

Mofakhami et al. [14] reported, for Polyamide 66 reinforced by 30 wt% of short glass fibre, a range of weld ratios between 0.50 and 0.65, depending on the pressure during weld process and the initial

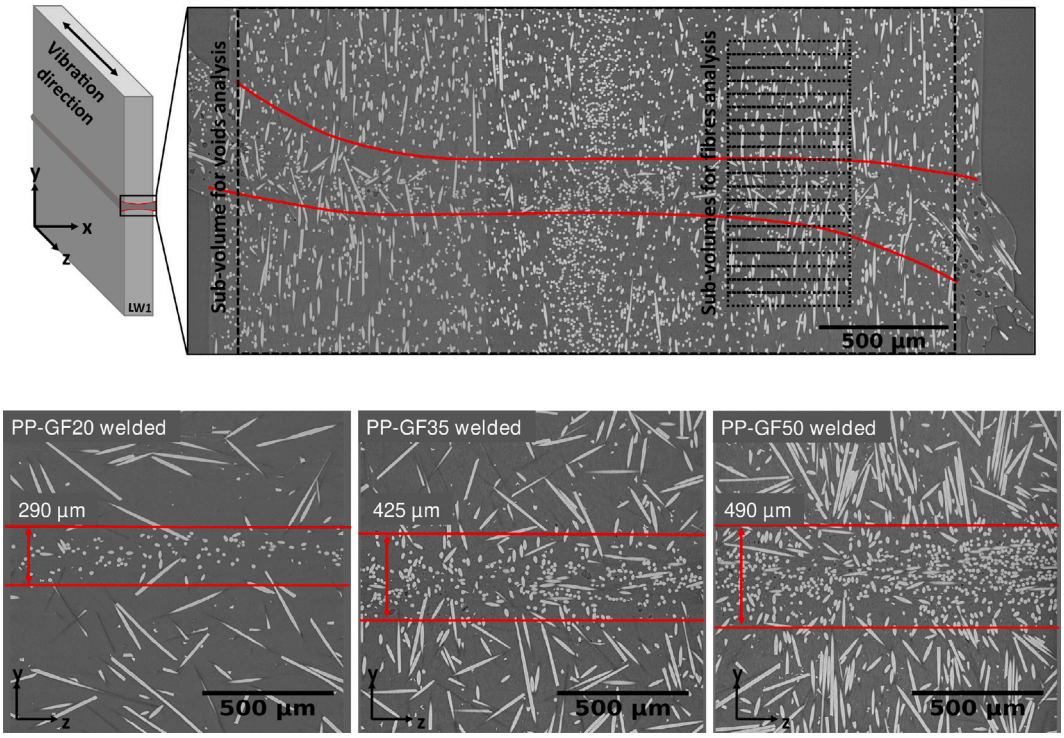

Fig. 2. Typical tomography image illustrating the regions of interest (top) and close-up within the welded region for different SGF concentrations (bottom). The typical weld thickness is obtained from observation of fibre reorientation (see discussion below).

orientation of the fibres. It was shown that the maximum stress was systematically equal to the stress at break. In addition, for non-reinforced thermoplastics, the weld ratio was close to unity.

Fig. 3 displays the engineering stress–strain curves of base and welded materials. As mentioned above, for welded specimens, the gauge length contained heterogeneous materials placed in series: the weld surrounded by base materials. Theoretically, the matter inside the gauge length cannot be considered as a representative volume element. These plots are not at the same scale, to clearly show the difference in the shape of the curves. For the sake of clarity, diamond symbols refer to the base material samples whereas squares correspond to welded ones. In addition, the last experimental point being representative of the failure of the tested specimen, the final drop in stress is characterised by the vertical line at the end of each plot, thus giving the stress and strain at break. As a matter of fact, the heat build-up associated with the thermomechanical response of the material was not considered [33].

It can be observed in Fig. 3 that the (visco)-elastic parts coincide regardless of the fibre content, meaning that the apparent Young's modulus was approximately the same for base (E^B) and welded (E^W) materials in this configuration. A concept of weld coefficient based on the Young's moduli is then introduced here as:

$$W_c^E = \frac{E^W}{E^B} \tag{6}$$

Furthermore, the engineering stress (σ_e) and the corresponding strain ($\varepsilon(\sigma_e)$), where the two stress–strain curves started to separate, were identified. The aforementioned characteristic values are summarised in Table 1.

Beyond σ_e and apart from PP-GF0, the shape of the stress–strain curves differed between the base and the welded samples. Indeed, whereas the welded samples exhibited stress softening, the base material showed approximately the same values of the maximum stress and the stress at break. These two characteristic stresses and the corresponding strains were studied in Appendix A.

Focusing first on the non-reinforced PP-GF0 (Fig. 3a), the maximum stress of the base sample is approximately the same as the stress at break of the welded one. However, the shape of the base material stress–strain curve exhibited stress softening after the maximum stress, the stress at break was therefore lower than the maximum stress. The weld ratio based on the maximum stresses ($W_c^{\sigma_{max}}$ in Eq. (5)) is similar to that reported in the literature: close to unity. It should however be noted that the maximum stress was not obtained at the same strain: 0.055 and 0.08 respectively for welded and base samples.

Table 1
Common characteristic values for base and welded samples.

Material	E^B (MPa)	E^W (MPa)	Wc^E (-)	σ_e (MPa)	$\varepsilon(\sigma_e)$ (-)
PP-GF0	1900	1800	0.95	22	0.019
PP-GF20	4100	3950	0.96	15	0.004
PP-GF35	6600	6500	0.98	34	0.006
PP-GF50	9000	8000	0.88	23	0.003

As already mentioned, conversely to the situation for unreinforced PP-GF0, the welded samples showed stress softening, whereas the base materials exhibited the same value of the maximum stress and stress at failure.

The trends observed in Table 1 are illustrated in Fig. 4. As a function of the fibre content, the evolution of the Young's moduli and the corresponding weld coefficient (W_c^E) were detailed in Fig. 4a, respectively in the first (left) and in the second (right) Y-axes. The Young's modulus showed the same value for both samples, leading to W_c^E close to unity in spite of a slight scatter at the last point (PP-GF50). Additionally, Fig. 4b plots the evolution of the stress corresponding to the deviation of both stress–strain curves (σ_e: first Y-axis), and the corresponding engineering strain ($\varepsilon(\sigma_e)$: second Y-axis). It can be noticed that while σ_e was constant with a large scatter, $\varepsilon(\sigma_e)$ showed a significant drop from PP-GF0 to PP-GF20 followed by a plateau with a large scatter.

Experimental data beyond σ_e consisted of the strength (σ_{max}), the stress at break (σ_{break}), and the corresponding strains, respectively $\varepsilon(\sigma_{max})$ and $\varepsilon(\sigma_{break})$, for the base and the welded materials.

Taking advantage of the characteristic values, all gathered in Appendix A, other weld coefficients were introduced, following the common one in Eq. (5):

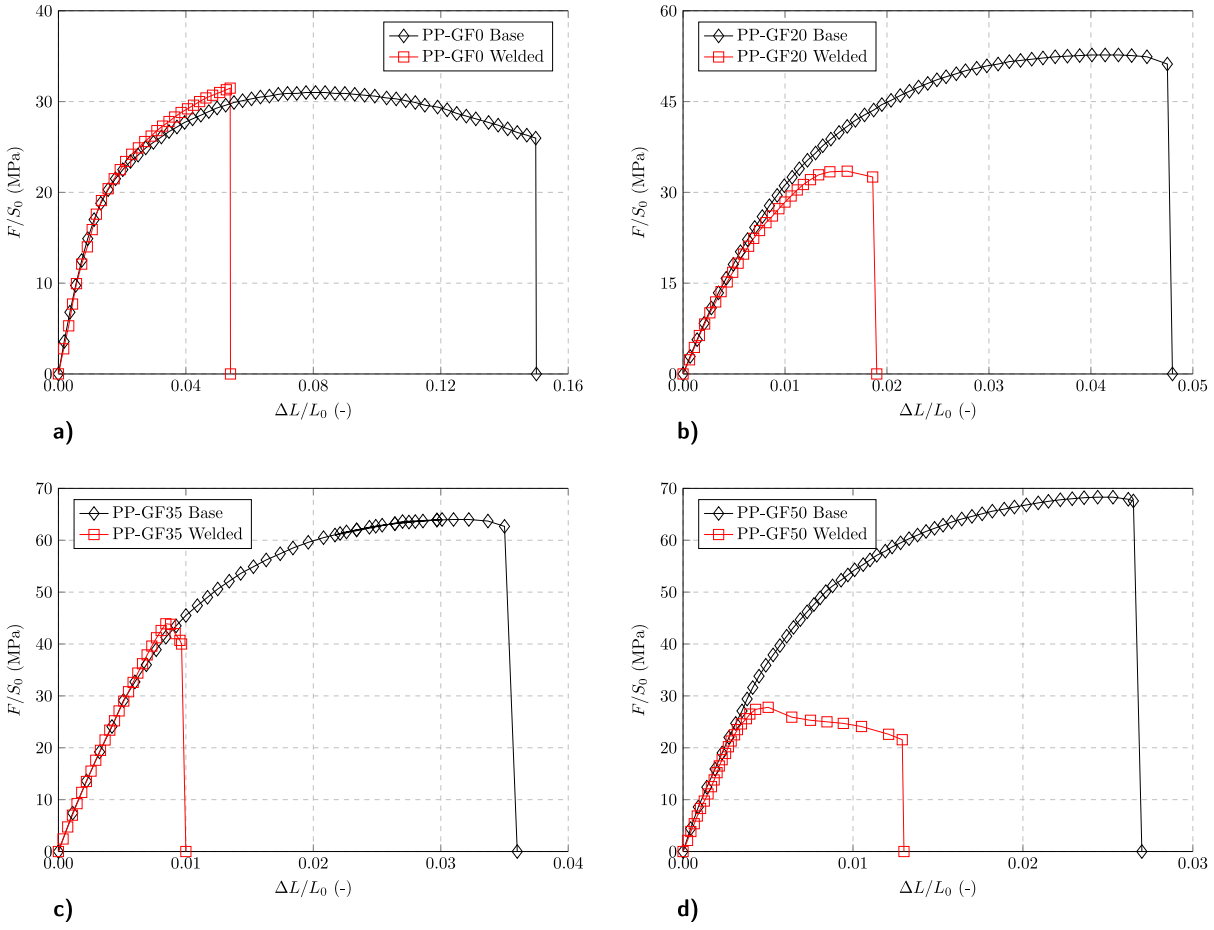

Fig. 3. Engineering stress–strain curves for base materials and welded samples: (a) PP-GF0, (b) PP-GF20, (c) PP-GF35, and (d) PP-GF50.

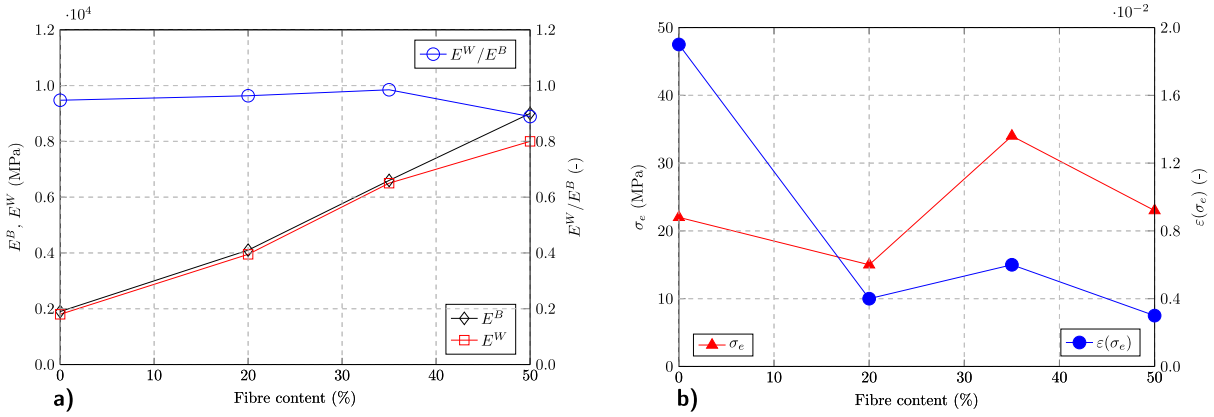

Fig. 4. Evolution of characteristic parameters as a function of the fibre content: (a) Young's moduli (E_B, E_W) and (E_W/E_B) ratio; (b) σ_e and the corresponding $\varepsilon(\sigma_e)$ (See Table 1).

- The weld coefficient based on the strain at maximum stress:

$$W_c^{\epsilon_{max}} = \frac{\epsilon(\sigma_{max}^W)}{\epsilon(\sigma_{max}^B)} \tag{7}$$

It can give an idea of the evolution of the strain ratio which accompanied the loss of strength when welding, or an increase, in the corresponding strain;

- The weld coefficient based on the stress at break:

$$W_c^{\sigma_{break}} = \frac{\sigma_{break}^W}{\sigma_{break}^B} \tag{8}$$

This one is to check if the loss of stress at break is of the same order of magnitude of that of the strength. This allows the presence of stress softening/hardening to be characterised (when the strength differs from the stress at break);

- The weld coefficient based on the strain at break:

$$W_c^{\epsilon_{break}} = \frac{\epsilon(\sigma_{break}^W)}{\epsilon(\sigma_{break}^B)} \tag{9}$$

The same concept as $W_c^{\epsilon_{max}}$ in Eq. (7) but corresponding to the strain at break.

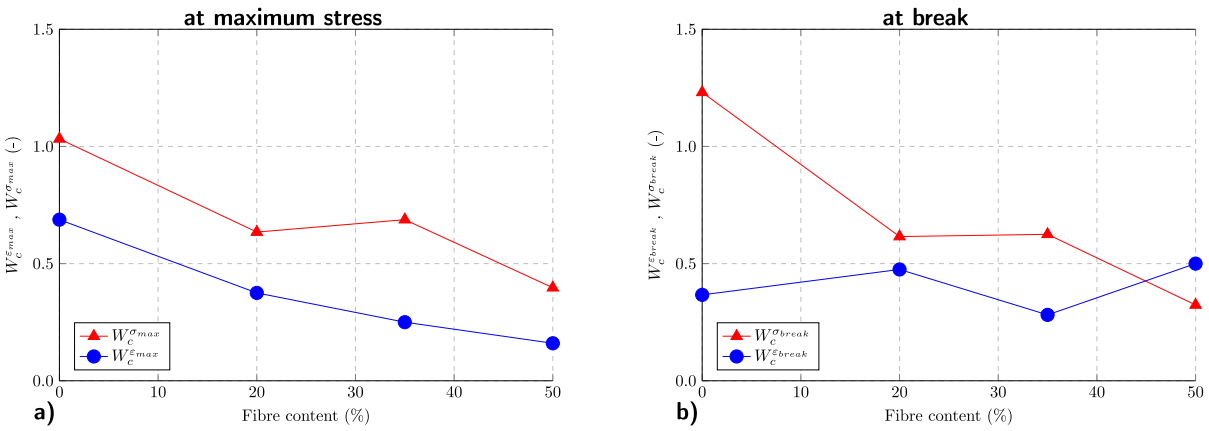

Fig. 5. Evolution of the Weld coefficients: (a) at σ_{max}, and (b) at σ_{break}.

Figs. 5a–b, illustrate the evolution of the four weld coefficients based on the stresses and the corresponding strains. The evolution of the classical weld coefficient $W_c^{\sigma_{max}}$ can be observed in Fig. 5a (full triangle symbols). The effect of adding 20% of short glass fibre from unreinforced material induced a decrease of the weld coefficient from unity to 0.63, whereas increasing the fibre content from 20% to 50%, disregarding an "irregularity" of PP-GF35, resulted in a decrease of $W_c^{\sigma_{max}}$ from 0.63 to 0.40.

For $W_c^{\epsilon_{max}}$ (full circles), the evolution consisted of a continuous decrease. The initial value for PP-GF0 being 0.7, the strain corresponding at the maximum stress is decreased of 30% due to the welding, which contrasted with the observation on the maximum stresses (no loss). Adding 20% of short glass fibres resulted in a decrease of $W_c^{\epsilon_{max}}$ down to 0.4. When the fibre content increases from 20% to 50%, the gradual decrease of $W_c^{\epsilon_{max}}$ continued down to 0.2. It can be concluded that adding reinforcement and increasing the fibre content induce a continuous decrease of the strain at the maximum stress of a welded sample.

Concerning the weld coefficients at the failure, in Fig. 5b, the specific point of $W_c^{\sigma_{break}}$ at 1.2 for PP-GF0 is due to the stress softening observed in the base material and not in the welded sample (see Fig. 3a). Then, conversely for reinforced materials, the welded samples did exhibit stress softening, but not the base material. $W_c^{\sigma_{break}}$ showed the same trend as $W_c^{\sigma_{max}}$ with the same irregularity for PP-GF35, with a slightly lower level for $W_c^{\sigma_{break}}$ due to the above-mentioned stress-softening.

For $W_c^{\epsilon_{break}}$ (full circles), apart from PP-GF35, a slight increase from 0.4 to 0.5 was highlighted with an increase of the fibre content.

In summary, increasing the fibre content was linked to a decrease in strength, stress at break and strain at the maximum stress. However, these comments were based on data at the macroscopic scale such as the engineering stress and strain. The welded samples being composed of three parts inside the "macroscopic" gauge length, local measurements of the strain were carried out, so as to better understand its partition within the two involved materials.

3.1.2. *Weld mechanical properties*

The welded samples – composed of the weld joint at mid-height surrounded by the base materials on both sides – are actually three specimens in series constituted of two materials. For these samples, the applied load is transmitted to the entire "structures" whereas the local deformations are expected to be different. To better analyse this heterogeneity of deformations, DIC technique was used (Section 2.6). The following investigations focused on the welds: Weld-GF0, Weld-GF20, Weld-GF35 and Weld-GF50, at the local scale. The base materials (PP-GF0, PP-GF20, PP-GF35, PP-GF50) will be analysed at both global and local scales.

Fig. 6 illustrates the approach allowing the local engineering strains to be accessed, in addition to $\Delta L/L_0$. This sketch, corresponding to the welded PP-GF35, is representative of all the welded specimens. The top graph was extracted from Fig. 3c, focusing on the "global" stress–strain curve of welded PP-GF35. The red circular flags, containing a number, relate the steps in the stress–strain curve to the pictures of the deformed specimen where speckle was set so as to use the DIC technique. Both local longitudinal $\delta l/l_0$ and transverse $\delta w/w_0$ strains were measured. The two VOIs' represented by the black and red rectangles, in flag number 3, correspond to the base material and the weld, respectively. Strain gradient in the width direction might appear (see Fig. 6 flags number 2 to 4), in this case the average value was assigned to the weld VOI. The contour map of the local strain is presented in the image of deformed specimen at each step in the stress–strain curve. The scale bar at the left of the viewgraphs shows the amount of the local longitudinal strain. It is to be mentioned that concerning the three layers of materials in series in the welded sample:

- the measured load, and therefore the engineering stress, is homogeneously exerted in all the three VOIs' composed of two base materials and the weld;
- the total longitudinal strain is assumed to be equal to the sum of the local strains such that $\Delta L/L_0 = 2(\delta l/l_0)^B + (\delta l/l_0)^W$.

The two graphs at the bottom of Fig. 6 show the local engineering stress–strain curves for the base material (left, black-filled diamond) and the weld (right, red-filled rectangle). It clearly appeared that strain localisation occurred very early in the weld. An amplification of the deformation with a factor 10 can be observed within the weld, for the same stress level. Furthermore, the failure occurred systematically in the weld after the above mentioned significant local deformation. This approach was applied on all the materials under study.

Fig. 7 is composed of global and local engineering stress–strain curves, relative respectively to $\Delta L/L_0$ as presented in Fig. 3 and $\delta l/l_0$ from DIC technique. The left column displays the whole curves whereas a closer look at small strains is proposed in the right column. For the sake of clarity, diamond symbols represent the base materials and the squares are related to the weld ones. The open symbols correspond to the response of the base material (unwelded specimens) whereas the fulled ones correspond to the base and welded material from the welded specimens; therefore, full symbols correspond to curves using the local strains ($\delta l/l_0$).

The plots have the same scale in the Y-axis, allowing a better comparison of the shapes of the stress–strain curves:

- in Fig. 7a, PP-GF0 showed a gradual stress softening and a strain at break greater than that of the weld (red full square);
- for PP-GF20/35/50 in Figs. 7c/e/g, by contrast, the gradual stress softening and the higher strains at break belong to the weld materials.

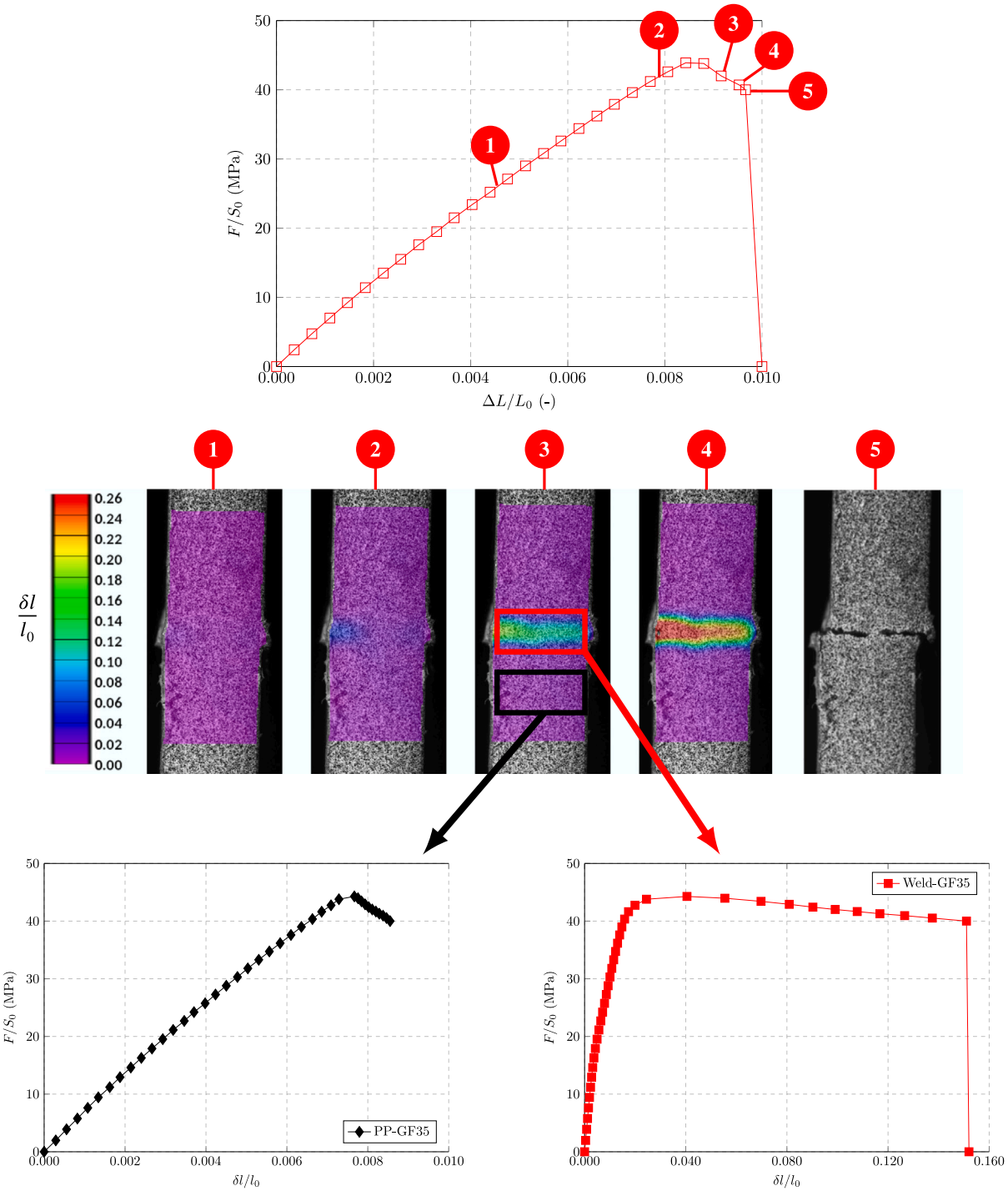

Fig. 6. PP-GF35 imaged at different stages of the tensile test with the corresponding $\delta l/l_0$ strain field obtained by DIC.

Regardless the fibre content, the (visco)-elastic responses of the global and local base materials (open and full black diamonds) were the same. The only difference between these two curves was that the global stress–strain curve went to the failure of the specimen, but for the local base material, the engineering stress saturates at the maximum stress of the weld. The stress softening observed on the weld is characterised by a stress decrease in the local base material. Figs. 7b-d-f-h showed the trends of the apparent local Young's moduli E^B for base material and E^W for the weld depending on the fibre content. These two characteristic local values are studied in Appendix B. The corresponding values of the local strains both at the ultimate strength and at break, respectively $\varepsilon(\sigma_{max})$ and $\varepsilon(\sigma_{break})$, were also gathered.

Taking advantage of the local characteristic values at the weld, additional weld coefficients are plotted in Fig. 8. Similar to the structure of the last subsection, the interpretation will be divided in two parts: (i) from Weld-GF0 to Weld-GF20, dedicated to the effect of the reinforcement; (ii) from Weld-20 to Weld-50, dealing with the effect of an increase of the fibre content.

Young's moduli

The weld coefficient related to the local Young's moduli W_c^E (Eq. (6)) is illustrated in Fig. 8a. For neat PP (PP-GF0) the welding process tends

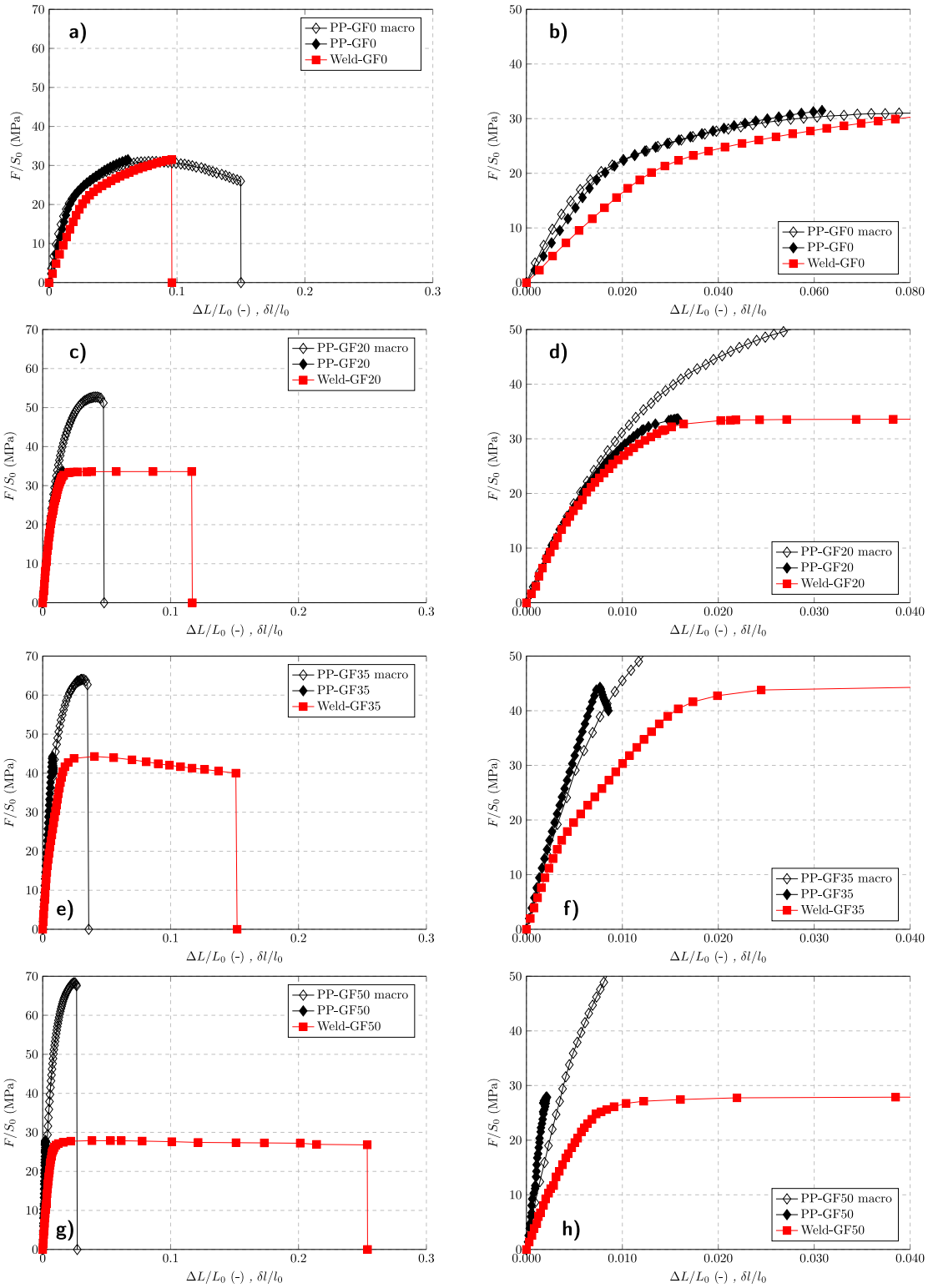

Fig. 7. Engineering stress–strain curves. Comparison between global (base material) and local (base and weld) data: (a–b) PP-GF0 and Weld-GF0; (c–d) PP-GF20 and Weld-GF20; (e–f) PP-GF35 and Weld-GF35; (g–h) PP-GF50 and Weld-GF50.

to soften the weld material leading to $W_c^E \simeq 0.65$, *i.e.* a loss of stiffness of 35%. Adding 20% of fibre content resulted in a stiffening of both materials so that $W_c^E \simeq 0.95$. In other words, the welding process for PP-GF20 resulted in softening the weld to about 5% only.

The effect of an increase in the fibre content from 20% to 50% is a continuous decrease of the weld coefficient W_c^E. The welding process for PP-GF35 and PP-GF50 induced a loss of stiffness of 30% and 70%, respectively.

Strains at ultimate strength of the weld

In Fig. 8b the weld coefficient linked to the strain at the ultimate strength of the weld $W_c^{\epsilon_{max}}$ is presented. This coefficient deals with the ratio between the strain in the weld and that in the VOI of the base material when the same ultimate strength is applied in both VOIs'. The

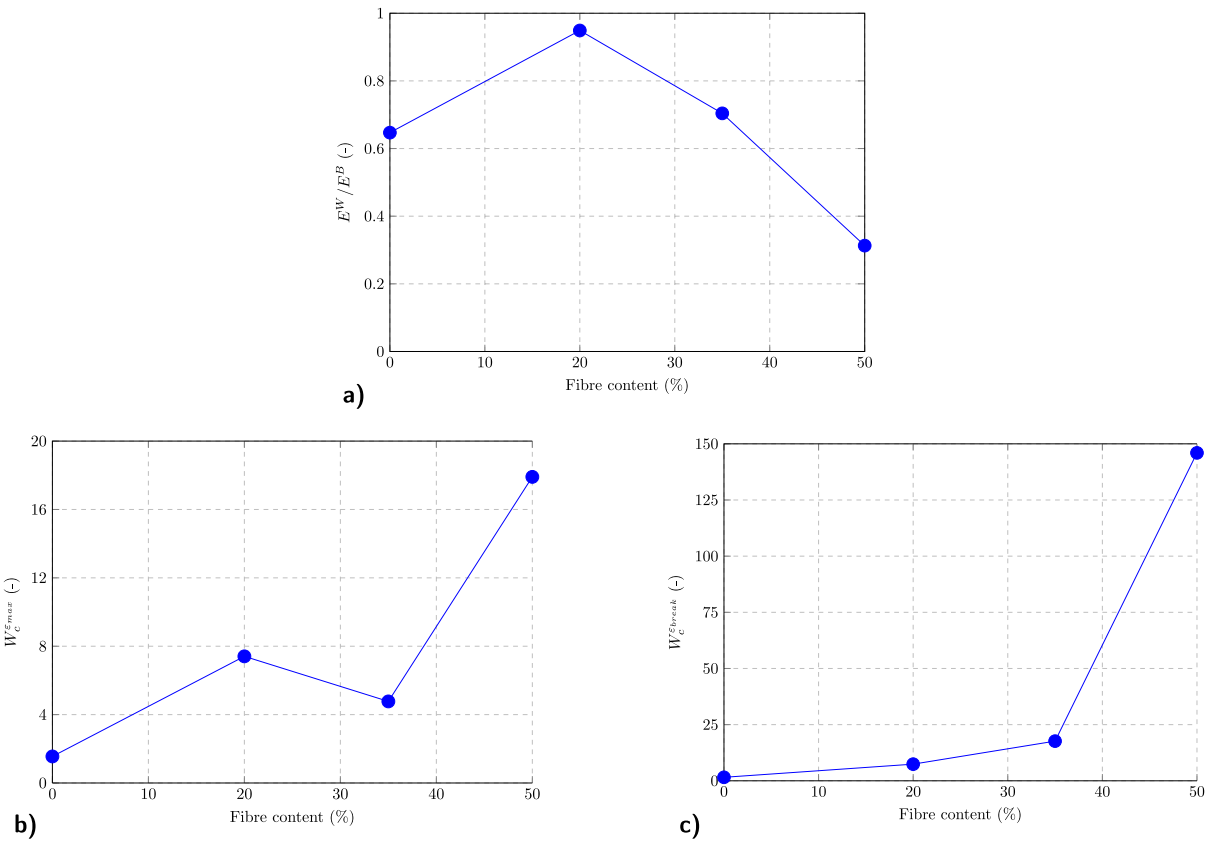

Fig. 8. Evolution of the local characteristic parameters as a function of the fibre content: (a) E_W/E_B ratio, (b) weld coefficient based on the strain at the maximum stress $W_c^{\varepsilon_{max}}$, and (c) weld coefficient based on the strain at break $W_c^{\varepsilon_{break}}$.

evolution of the weld coefficient $W_c^{\varepsilon_{max}}$ with the fibre content is always greater than 1. This means that the presence of the weld leads to an amplification of the deformation within it. For the neat PP-GF0, the amount of this deformation amplification is about 1.5. But it increases to an average value as high as 6 when increasing the fibre content to 20 and 35%. At last, Weld-GF50 shows a drastic increase of $W_c^{\varepsilon_{max}}$ up to 17.

Strains at break of the weld

The evolution of the weld coefficient at break $W_c^{\varepsilon_{break}}$, ratio between the strain in the weld and in the base material, with respect to the fibre content is shown in Fig. 8c. Its value starts at 1.5 for Weld-GF0 and exponentially increases to reach 145 for Weld-GF50. Once again, it can be concluded that the presence of the weld leads to an amplification of the deformation within. Furthermore, the strain is gradually transferred to the weld for increasing fibre content.

The above mentioned amplification of the deformation was observed on the local longitudinal strain $\delta l/l_0$ at the welded area. The DIC technique giving access to the local transverse strain $\delta w/w_0$, both the Poisson's ratio ν and the volume change $\Delta V/V_0$ can be deduced as follows:

$$\nu = -\frac{\frac{\delta w}{w_0}}{\frac{\delta l}{l_0}} \tag{10}$$

$$\frac{\Delta V}{V_0} = \frac{\delta l}{l_0} + 2\frac{\delta w}{w_0} \tag{11}$$

The evolution of both variables is studied in Appendix B, only the values at two specific events (yield and failure) are summarised in Table 2.

Fig. 9 illustrates the effects of increasing fibres contents on the Poisson's ratio (left Y-axis) and the associated volume variation (right Y-axis) at the yield (Fig. 9a) and at break (Fig. 9b). The amplification of the longitudinal strain is linked to a volume variation corresponding to a decrease of ν from 0.5 – see Appendix B – the objective here is to analyse which of the yield stress and the stress at break is the more sensitive to this volume variation.

Table 2
Poisson's ratio ν and volume change $\Delta V/V_0$ at the weld joint.

Weld	Position	ν (-)	$\Delta V/V_0$(-)
Weld-GF0	Maximum σ_{max}	0.5	0
	Break σ_{break}	0.5	0
Weld-GF20	Maximum σ_{max}	0.5	0
	Break σ_{break}	0.2	0.07
Weld-GF35	Maximum σ_{max}	0.14	0.02
	Break σ_{break}	0	0.15
Weld-GF50	Maximum σ_{max}	0.09	0.04
	Break σ_{break}	0	0.25

In Fig. 9a the Poisson's ratio of Weld-GF0 is estimated at 0.5 corresponding to zero volume change at the yield. The welded PP-matrix is then considered as incompressible, thanks to these data. The same situation is encountered for Weld-GF20, meaning that adding 20% of short glass fibres did not change the transverse response of the material at the yield. By increasing the fibre content from 20%, up to 50%, the Poisson's ratio drops down to reach 0.1. Accordingly, the volume change increases to reach a small value of 4% for Weld-GF50 at yield.

Considering the data at break, see Fig. 9b, every trend is gradual from 0 to 50% fibre content. In particular, for Weld-GF20, ν and $\Delta V/V_0$ are different from those of Weld-GF0 by opposition to the data at yield. A better sensitivity to fibre content was clearly obtained. From 35% of fibre content, the Poisson's ratio at break is zero – oedometric configuration – leading to a volume variation as high as 25%. From

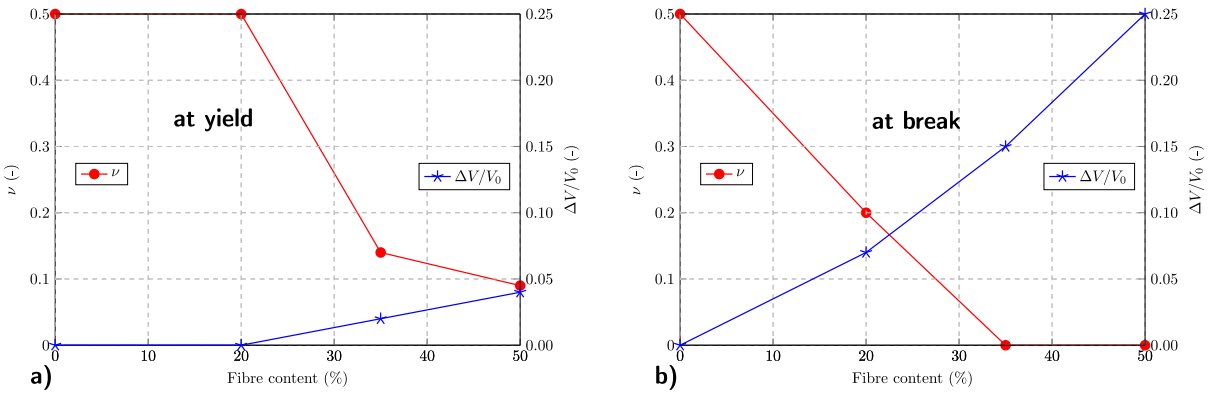

Fig. 9. Evolution of the Poisson's ratio (ν) and the corresponding volume variation ($\Delta V/V_0$) as a function of the fibre content: (a) at the yield stress; (b) at break.

Table 3
GPC and DSC values for unwelded and welded PP-GF0 and PP-GF35. M_w is the molecular weight, D_M is the polymer dispersity, T_f is the fusion temperature, and χ_c is the index of crystallinity.

		M_w (kg/mol)	D_M	T_f (°C)	χ_c
PP-GF0	Injected	539	6	163	52
	Welded	505	5.9	163	52
PP-GF35	Injected	542	5.9	163	51
	Welded	504	5.7	163	50

the authors' viewpoint, these data at the break of the weld are the most relevant to better understand the mechanisms of deformation and failure of the welded joint.

The main conclusions from this section can be summarised as follows:

- Taking into consideration the significant strain localisation within the weld and the corresponding consequences, a concept of weld coefficient based on the strain at break of the weld is recommended.
- An amplification of the longitudinal strain is observed because of an increase in the fibre content.
- The amplification of the strain is accompanied by a volume increase, once more when the fibre content increases.

The next subsection is dedicated to better understand the origin of the amplification of both the strain and the volume change thanks to the characterisation of the welded matrix and the analysis of the distribution of the short glass fibres through the given matrix.

3.2. Characterisation of the matrix

To dwell further into the mechanisms responsible for the strain localisation within the weld, a first scenario can be proposed, based on the local embrittlement of PP matrix. This embrittlement could be due to a chemical degradation of the polymer during the welding process: oxidation leads to chain scission and molecular weight drop. As a result, the polymer may become brittle if the molecular weight is below a critical molecular weight M_C, with M_C close to 200 kg/mol for PP [34]. Furthermore, the molecular weight drop can also lead to an increase of the index of crystallinity in the welded area [34]. To verify this hypothesis, the polymer matrix was characterised with both GPC and DSC measurements for the unfilled polymer (PP-GF0) and the PP-GF35 (Table 3).

From GPC, it appeared that there is only a slight decrease in the average molecular weight due to welding process, for both neat (PP-GF0) and reinforced (PP-GF35) materials. In other words, the slight decrease is not sufficient to decrease the molar mass below M_C. The values obtained before and after welding do not depend on the presence of the short glass fibres.

Isotactic polypropylene crystallises in two main forms, α and β which have melting temperatures between 160 and 175 °C and 145 and 169 °C, respectively [35,36]. The α-phase is the main crystalline form of PP and the amount of β-phase is never more than 10% of the polymer chains. From the DSC measurements, no significant changes can be identified either from the crystallinity degree, close to 50%, nor the crystalline morphology, since both the shape of the fusion peak and the fusion temperature T_f remain unchanged (one peak at 163 °C which characterised the α-phase, data not shown).

These results are in accordance with the conclusion, for PP-GF0, which highlights the same local stress–strain curves (Fig. 3a) for the base and weld materials, together with the weld coefficient related to Young's modulus equal to 1 (Fig. 4a). In consequence, from DSC and GPC measurements, changes in the matrix due to welding are of minor order. To go further about the strain localisation in the weld, the focus was put on the change in the arrangement of the short fibres (fibre content, fibre orientation) after the welding process.

3.3. Fibre reorganisation due to the welding process

The observation of the microstructure was performed by 3D imaging from Synchrotron Radiation Computed Tomography (SRCT) data set (Fig. 2).

3.3.1. Fibres volume fraction

The movement of the fibres during welding can be evaluated by measuring their "density" along the longitudinal direction; thus crossing the three layers Base/Weld/Base material. From the fibres volume fraction, the weight fraction can be determined by using the density of glass fibre and PP. Assuming typical values of 2.5 g/cm^3 and 0.9 g/cm^3, the average values for PP-GF20, PP-GF35 and PP-GF50 are respectively 19.4, 34.6 and 47. wt%, in good agreement with the theoretical ones. Fig. 10a illustrates the evolution of the density of fibres along the longitudinal path for the three reinforced PP. It is clearly shown that the weld (noted as Weld-GF in Fig. 10a) exhibits higher level of fibre density than the base material (PP-GF) in both sides of the weld. Furthermore, the higher the fibre content, the higher the density of the fibres within the weld. The domains of base (PP-GF) and weld (Weld-GF) materials are delimited by dashed vertical lines.

Fig. 10b displays the increase of the maximum fibre density with respect to increasing fibre content. The fibre density, in the left Y-axis, of the PP-GF and Weld-GF is represented as open diamond and open square symbols, respectively. Moreover, the thickness of the weld is also increasing with the fibre content (right Y-axis in Fig. 10b). Therefore, the higher the fibre content, the larger the volume with higher fibre density.

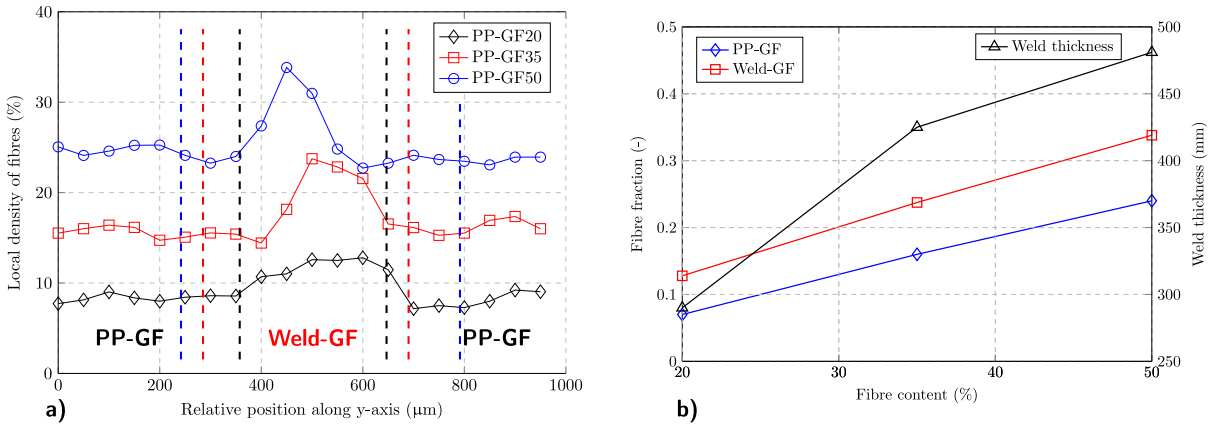

Fig. 10. Density of the fibres: (a) evolution of the density along the longitudinal direction for PP-GF20/35/50; (b) evolution of the maximum density in the weld as a function of the fibre content.

A higher density of fibres induces a smaller inter-fibre distance. At the microstructure scale, the inter-fibre distance can be considered as a local gauge length (l_0) for the material located between two fibres. Reducing this gauge length in the weld implies amplification of the longitudinal strain. For natural rubber with carbon black fillers, the same effect was reported for a higher density of carbon black [37].

3.3.2. *Reorientation of fibres*

To establish the fibre reorientation during welding, the diagonal terms of the orientation tensor Eqs. ((2)–(3)–(4)) were calculated in each subvolume as illustrated in Fig. 2. Note that the injection direction coincided with the longitudinal one in the specimen and therefore related to a_{yy}. Accordingly, a_{xx} and a_{zz} characterise the transverse plane, for which the normal vector is supported by a_{yy}. These diagonal terms represent the probability that the fibres are oriented in the corresponding direction.

Fig. 11 illustrates the evolution of a_{xx}, a_{yy} and a_{zz} with respect to the relative position in the y-axis (both injection and loading direction). Each graph is associated with a fibre content: 20, 35 and 50%. The domains of base (PP-GF) and weld (Weld-GF) materials are delimited by two dashed vertical lines. The above mentioned increase of the weld thickness as a function of the fibre content can then be noticed in the three graphs.

In the base materials (PP-GF), a_{yy} (open squares) is the most significant contribution due to the injection direction. It can be noticed that this contribution increases with the amount of fibre content. The contribution of a_{xx} (open diamonds), in the thickness direction, was in all cases very small or even null. At last, a_{zz} (open circles), related to the vibration direction, complements to 1 the trace of the orientation tensor. In summary, the fibres in the base materials are in the y–z plane with a major contribution towards the injection direction represented by a_{yy}.

The welding process made these distributions change into what was noticed in the weld materials as commented in the following. The most spectacular observation is the drop of a_{yy}, compensated essentially by an increase in a_{xx}. The a_{zz} component, fraction of fibres in the vibration direction, remains more or less constant. In the welds, $a_{xx} \simeq a_{yy} \simeq a_{zz}$, so that approximately 2/3 of the fibres are within the x–z plane. The welding process made the longitudinal fibres rotate of about 90° so as to locate them close to the transverse x–z plane. The significant increase in a_{xx} comes from the x-component of the aforementioned rotation. It can then be concluded that, regardless of the fibre content, the base material contains fibres in the loading direction, whereas the weld is composed of fibres in the weld plane.

During the tensile tests, the base materials in both sides of the weld show transverse contraction corresponding essentially to the Poisson's ratio of the matrix; the orientation of the fibres being in the tensile direction. In the weld, the transverse deformations are applied parallelly to the fibres orientation, therefore more fibres are implied than on the base material, limiting the transverse strain. At the "percolation" of the fibres, zero transverse is expected to occur, corresponding to zero Poisson's ratio as encountered in (Fig. 9b) for higher fibre contents. All along the stage of deformation where the transverse strain – hence the Poisson's ratio – is small enough whilst the amplified longitudinal strain is still increasing, the matrix is confined (or bonded) inside two rigid blocks (set of fibres) which move away from each other. This configuration is similar to oedometric traction [38] for the matrix, giving raise to a triaxial stress state that can result in cavity nucleation. The volumetric strain or the volume change significantly increases as noticed in Fig. 9b. The growth and coalescence of these nucleated microscopic voids – and the pre-existing ones – provoke the failure of the weld. These mechanisms are enhanced for large volume involved, like in Weld-GF50.

To conclude, increasing the fibre content leads to an amplification of the longitudinal local strain due to a decrease in the gauge length (inter-fibre distance), associated with a volume change coming from the tension on confined matrix, in the weld.

3.3.3. *Cavitation distribution in the weld zone*

The Synchrotron tomography data set showed the presence of pre-existing voids. This subsection addresses the evolution of these voids (growth an coalescence), during the deformation of the sample before failure. Moreover, the mechanisms of nucleation of new voids are qualitatively investigated so as to relate the overall void growth to the aforementioned volumetric strain.

Initial distribution of porosity

Following the analysis performed in [14], Fig. 12 shows the cavities in a volume of interest surrounding the weld (see Fig. 2) obtained for the PP-GF35 sample, assumed to be representative of the other welded samples in terms of porosity distribution. Fig. 12a shows a slice at approximately mid-width of the tomographic data set. The orientation of fibres mentioned in Fig. 11 is illustrated, together with some initial porosity essentially located at both sides of the samples where the fibre orientation is "perturbed". These cavities can be attributed to flow instabilities occurring in the melt while fibres reorient during welding, as discussed in [39].

The three yellow arrows labelled IP indicate some "Initial Porosity" (IP) which differ in their location, morphology and number with a cluster. In particular, the deepest initial pores corresponding to this slice were indicated by the yellow arrows in the middle position. In the central part through the thickness – where the fibres were oriented perpendicularly to the longitudinal direction – no initial porosity was observed. An attempt was made, in Fig. 12b, to digitise the porosity so as to illustrate the characteristics of pores in a top view plane.

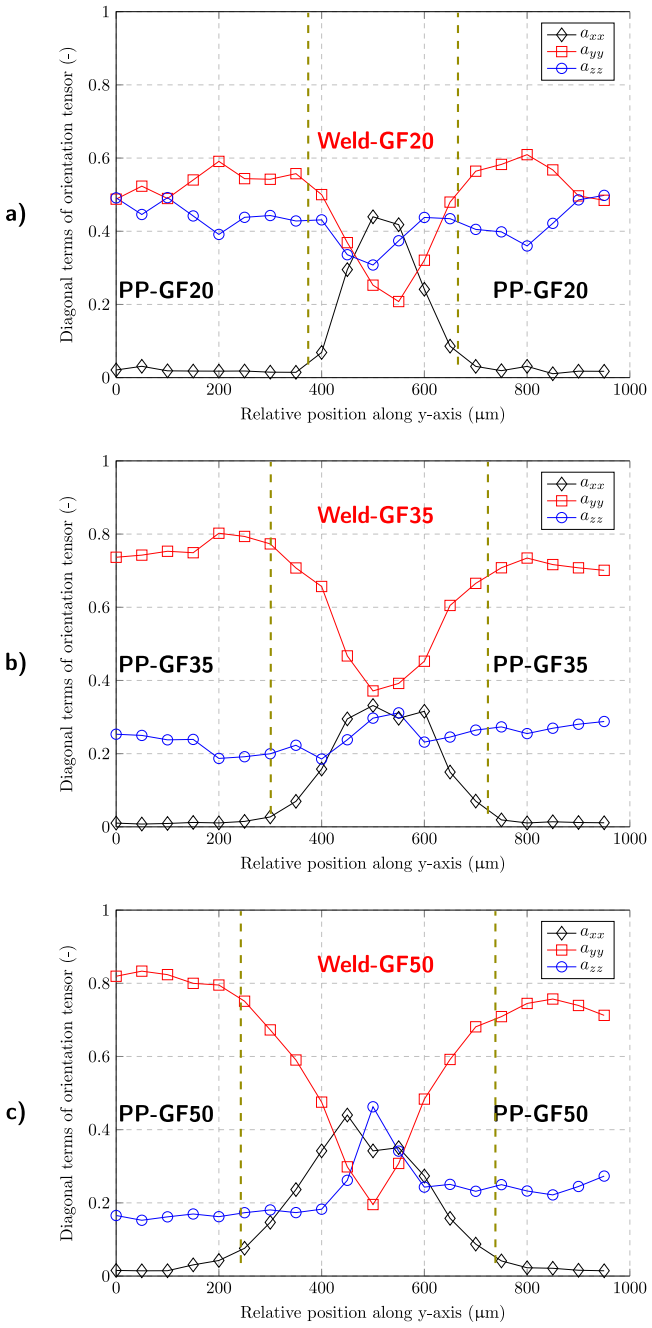

Fig. 11. Evolution of orientations of the fibres along the longitudinal direction: (a) PP-GF20; (b) PP-GF35; (c) PP-GF50.

This figure shows in a better way the morphology and distribution of porosity:

- Maximum void is located in both sides near the lateral surfaces.
- A skin-core like effect was noticed near the surface, where a "M" profile can be seen instead of an homogeneous distribution of voids.

When calculating the void volume fraction (Total volume of voids divided by the whole volume of interest), it was evaluated at 0.05% for PP-GF35. The same value was obtained for PP-GF50, whereas a lower value of 0.004% was encountered for PP-GF20. On the first hand, it can be noticed that cavities are only visible in the weld. On the second hand, the void volume fraction increases drastically for PP-GF35 and PP-GF50 reaching a plateau value (respectively 0.05 and 0.04%), compared with the PP-GF20. Furthermore, the nature and size of the cavities also seem to differ in the PP-GF20 sample: The higher the fibre content, the higher the initial porosity level.

Evolution of porosity during deformation

For each fibre content, some tests were stopped well after the peak stress was reached, that is, in the region where the $\Delta V/V_0$ was increasing — see Appendix B, Fig. 17. The deformed samples were then examined using *ex-situ* SRCT scans, so as to compare the deformed with the initial microstructures.

Fig. 13 illustrates mid-width slices of data sets for PP-GF35 and PP-GF50 samples from interrupted tests. It can be noted that, at mid-width plane, through-thickness cracks were apparent in both samples. In particular, in the central region where no initial porosity was observed, aligned voids in the x-direction (coalesced or not) are now evidenced. Additionally, since these examinations were done on unloaded samples, only the residual opening of the crack can be observed. These voids correspond therefore to irreversible volume increase inducing positive volumetric strain noted as plastic dilation [40,41]. This local residual crack opening (height, thickness) was noticed to be smaller for PP-GF35 than for PP-GF50. Focus was put on Fig. 13a, corresponding to PP-GF35. Indeed, this sample was considered to allow the observation of the beginning of voiding phenomenon, compared with PP-GF50 where damage seemed to be more pronounced. Note that all kinds of "damage" (causing voiding of the matrix) in the composite materials, as reported by [42], could be found. Namely,

- Decohesion of the matrix at the fibres' ends as well as in the longitudinal direction;
- Fibre breaks through the cross section as well as longitudinally (not so much);
- Growth of pre-existing porosity;
- Crazes in the regions locally rich of matrix.

In Fig. 14, some closer views highlighting the essential of voiding mechanisms were extracted from Fig. 13a. The coordinate system is shown in Fig. 14a where the tensile direction is the y-axis. Fig. 14a was extracted from the central part (mid-thickness/mid-width) of the Weld-GF35. The fibres are oriented to the z-axis, perpendicular to the tensile direction. This is the worst configuration for the matrix located between two close fibres since it is subjected to a confined traction. This situation promotes quasi-equi-triaxial stress state [38] inducing: (i) void nucleation by fibre/matrix debonding; (ii) the void growth by triaxial stress state — crazing of the matrix. This slice being examined after unloading, the inter-void fibrils of the PP matrix are buckling. Furthermore, a large porosity constituted by the coalescence of crazes and fibre/matrix decohesion is illustrated in Fig. 14a.

Fig. 14b was extracted from the data set near the lateral surface (right end of Fig. 13a), where the reorientation of the fibres could be observed. Once more, fibre/matrix decohesion was observed regardless the direction of the fibres (x or z axes), still perpendicular to the tensile direction. Additionally, a series of crazes in the matrix can be observed. A cluster of initial porosity was also seen (indicated in the viewgraph).

Fig. 14c shows a magnification of the views at the left end of Fig. 13a. In addition to crazes and initial porosities, a coalescence of voids emanating from decohesion of 4 fibres oriented in the x-direction could be highlighted.

All of these voids contribute to plastic dilation in the microstructure, letting $\Delta V/V_0$ increase after the maximum stress as clearly shown in Fig. 9. Increasing the fibres content results in decreasing the inter-fibres distance in the central part of the weld, promoting then a weakness of the weld at this location. The level of the stress at break drastically decreases, causing the weld coefficient to be at a lower value.

Conclusions

Welded glass-fibre-reinforced polypropylene (GF-PP) was studied in-depth to better understand the reduction of the weld ratio, ratio

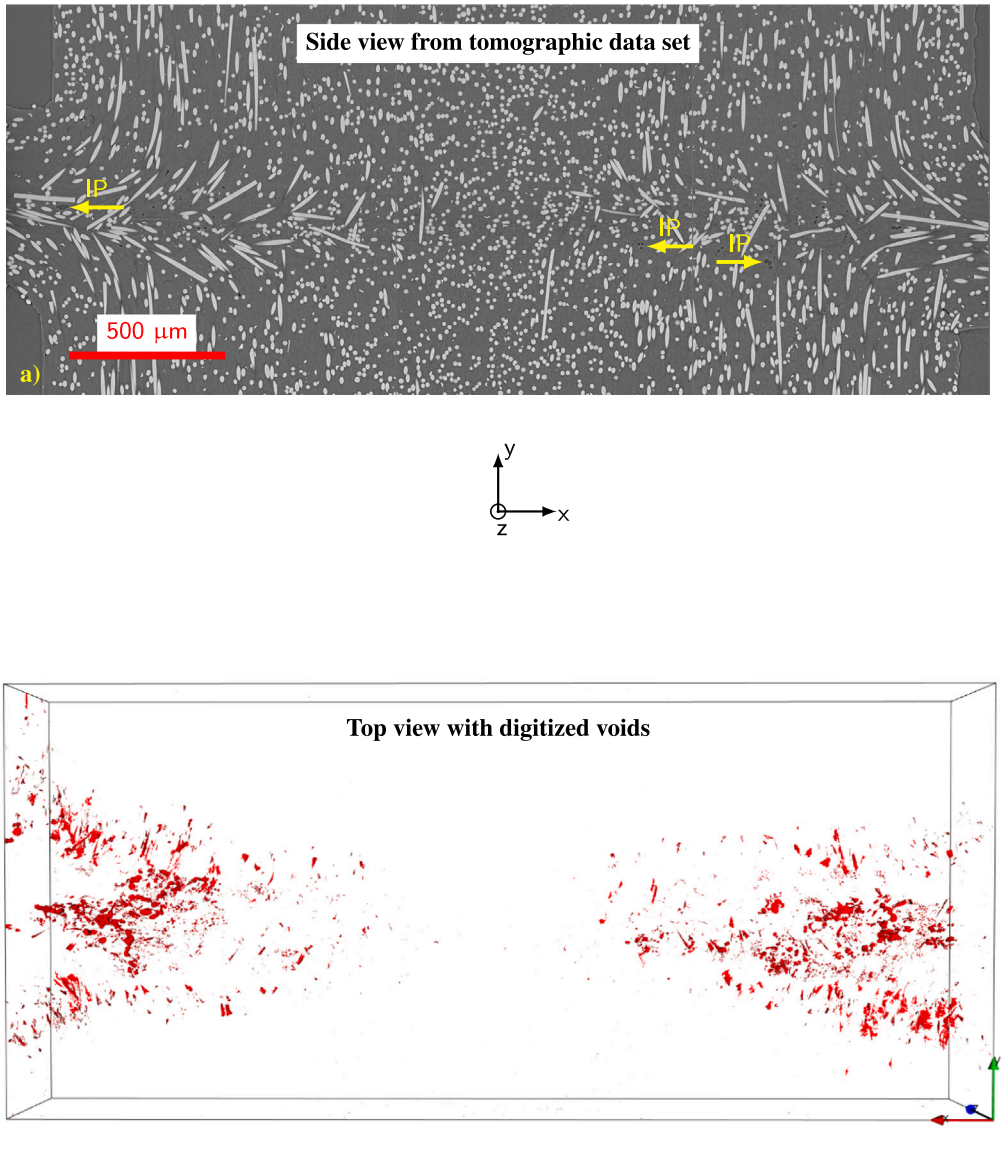

Fig. 12. PP-GF35 microstructure images with an attempt to estimate the initial porosity (IP): (a) Side views of the scanned data at mid-width plane; (b) Corresponding top view at mid-height with digitised porosity.

between the ultimate strength of the welded sample and that of the base material, within the framework of the relationship between the microstructural change and the mechanical properties.

It was shown that the welding process does not affect the physico-chemical characteristics of the matrix; therefore, the study focussed on the composite material. Increasing the fibre content on the welded material was linked with a decrease in strength, stress at break and strain at maximum stress up, respectively, to 60, 68 and 84% compared to unwelded material. However, these observations are based on macroscopic data.

The DIC technique was used to retrieve the local response at the welded zone. A strain-at-break weld coefficient, defined as the ratio between the local strain at the weld and the corresponding applied strain, was found to show a local magnification equal to 19.5. Using X-ray microtomography, the strain magnification could be explained by a higher fibre density at the welded zone — between 40 and 50%. Indeed, the higher the fibre content, the higher the confinement. In addition, fibres were orientated in the weld plane limiting the transverse strain. The transverse tension of confined material favours high stiffness and void nucleation, which can be considered as an irreversible volume variation, causing embrittlement of the welded material. This voiding drastically decreases the ultimate strength of the welded material and thus the weld ratio. In line with previous studies, the results could explain why a higher welding pressure, linked with a higher fibre density at the welded zone, is related with a loss of the mechanical properties.

Although DIC measurements are surface measurements – while the variation is volumetric – these results have already allowed to verify that the local deformation, at the weld, is significantly higher than the global one. Future work should include the study of the effects of improving the mechanical properties, e.g. reducing the pressure during welding [14]; however, simultaneous surface and volume studies, DIC and Digital volume correlation (DVC), would be necessary to understand the effects of porosity on the deformation distribution.

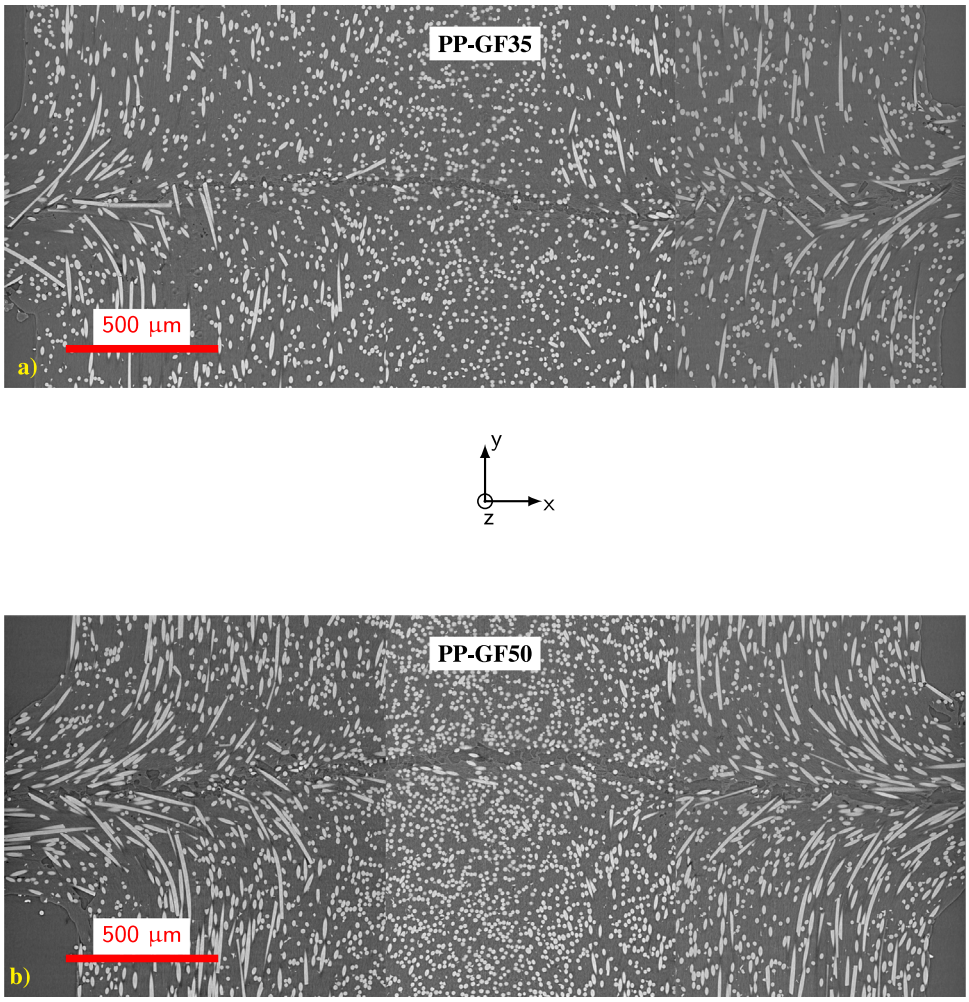

Fig. 13. Examinations at mid-width slices from SRCT data sets on sample where tests were interrupted post peak-load: (a) PP-GF35; (b) PP-GF50.

CRediT authorship contribution statement

E. Mofakhami: Methodology, Investigation, Formal analysis. **L. Gervat:** Conceptualization, Funding acquisition, Project administration, Supervision. **B. Fayolle:** Conceptualization, Writing – original & review, Supervision. **G. Miquelard-Garnier:** Conceptualization, Project administration, Funding acquisition, Writing – original & review, Supervision. **C. Ovalle:** Conceptualization, Formal analysis, Investigation, Data curation, Writing – original draft, Writing – review & editing. **L. Laiarinandrasana:** Conceptualization, Project administration, Funding acquisition, Writing – original & review, Supervision.

Declaration of competing interest

The authors declare that they have no known competing financial interests or personal relationships that could have appeared to influence the work reported in this paper.

Data availability

Data will be made available on request.

Acknowledgements

The authors are grateful to SOLEIL selection committee (Proposal number: 20180023). We want to thank all the scientific staff from ANATOMIX beamline, Timm Weitkamp, Mario Scheel and Jonathan Perrin. ANATOMIX is an Equipment of Excellence (EQUIPEX) funded by the Investments for the Future program of the French National Research Agency (ANR), project NanoimagesX, grant no. ANR-11-EQPX-0031. We also thank N. Dargere from Novarest for his help preparing the welded samples, as well as E. Richaud for performing the GPC measurements. Finally, we want to thank the ANRT for subsiding this PhD program (N° 2016/1216).

Appendix A. Characteristic values for base and welded samples

The strength, the stress at break, and the corresponding strains for the base and the welded materials are shown in Table 4. Note that in the nomenclature the subscripts *max* and *break* correspond, respectively, to maximum (strength) and value at break.

Fig. 15 displays, as a function of the fibre content, the maximum stress (strength), the stress at break and the corresponding strains. The scales of the ordinate axis were prescribed to be the same, so as to compare the values. Due to the inversion of the trend between unreinforced and reinforced polypropylene, the interpretation of the data was carried out in two folds depending on the fibre contents:

- from PP-GF0 to PP-GF20: the analysis dealt with the effect of reinforcement;
- from PP-GF20 to PP-GF50: the effects of the increasing value of fibre contents were investigated.

Figs. 15a-b compare the maximum stress and the stress at break for all materials. The welded samples exhibited scattered but constant values of the strength and the stress at break. The base materials showed

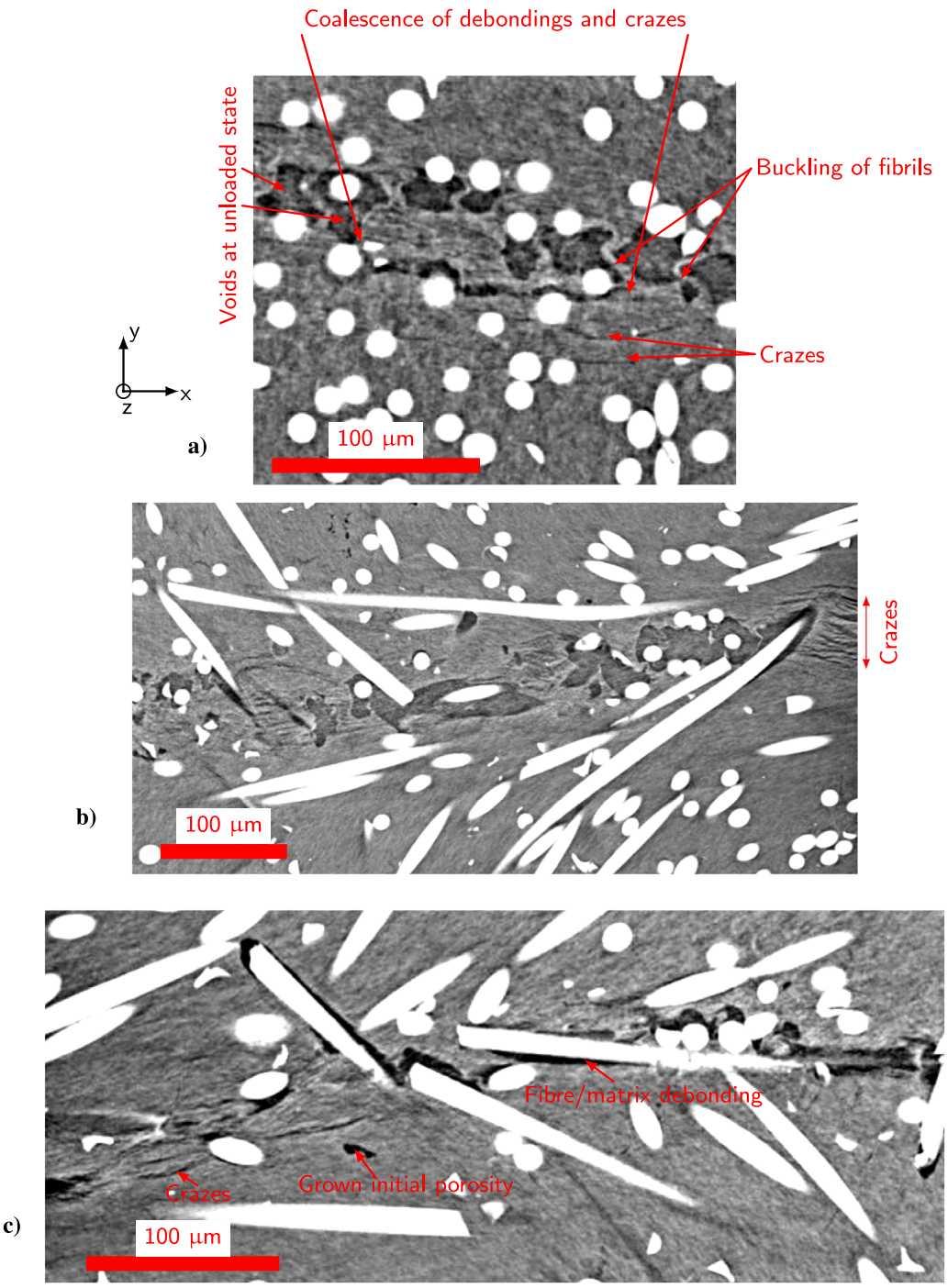

Fig. 14. Closer views of void nucleation and growth mechanisms in the PP matrix for PP-GF35: (a) Fibre/matrix decohesion in the central zone (fibres in the z-direction); (b) Crazes near the surfaces; (c) Fibre/matrix decohesion in the central zone (fibres in the x-direction).

increasing both maximum and stress at break with increasing fibre content. To go further into detail, for PP-GF0 (unreinforced polypropylene), the maximum stresses turned out to be the same (Fig. 15a), whereas the stress at break of the welded sample was higher than that of the base material. The effect of the reinforcement with 20% of fibre content can be summarised as an increase in the strength and stress at break for base materials. No effect can be observed on the welded samples: the strength and the stress at break were the same as those of welded PP-GF0.

For reinforced polypropylene (PP-GF20/35/50) the opposite situation was encountered. Indeed, the welded samples showed stress softening with clear peak stress (Fig. 3). It can be observed with open square symbols that σ^W_{max}, in Fig. 15a, is slightly greater than σ^W_{break}, in Fig. 15b. Contrary to base materials (open diamond symbols), the maximum stresses (Fig. 15a) were the same as the stresses at break (Fig. 15b). While, for base materials, both maximum stress and stress at break were continuously increasing with respect to the fibre contents – due to the reinforcement – the welded samples exhibited either constant or decreasing value of both stresses. The slight increase of these stresses for welded PP-GF35 could not allow clear conclusion.

Concerning the strains in Figs. 15c-d, a general decreasing trend with respect to increasing fibre content is observed. However, the drop in $\varepsilon(\sigma^B_{max})$ is more significant from PP-GF0 to PP-GF20 (effects of reinforcement addition) than from PP-GF20 to PP-GF50. This comment

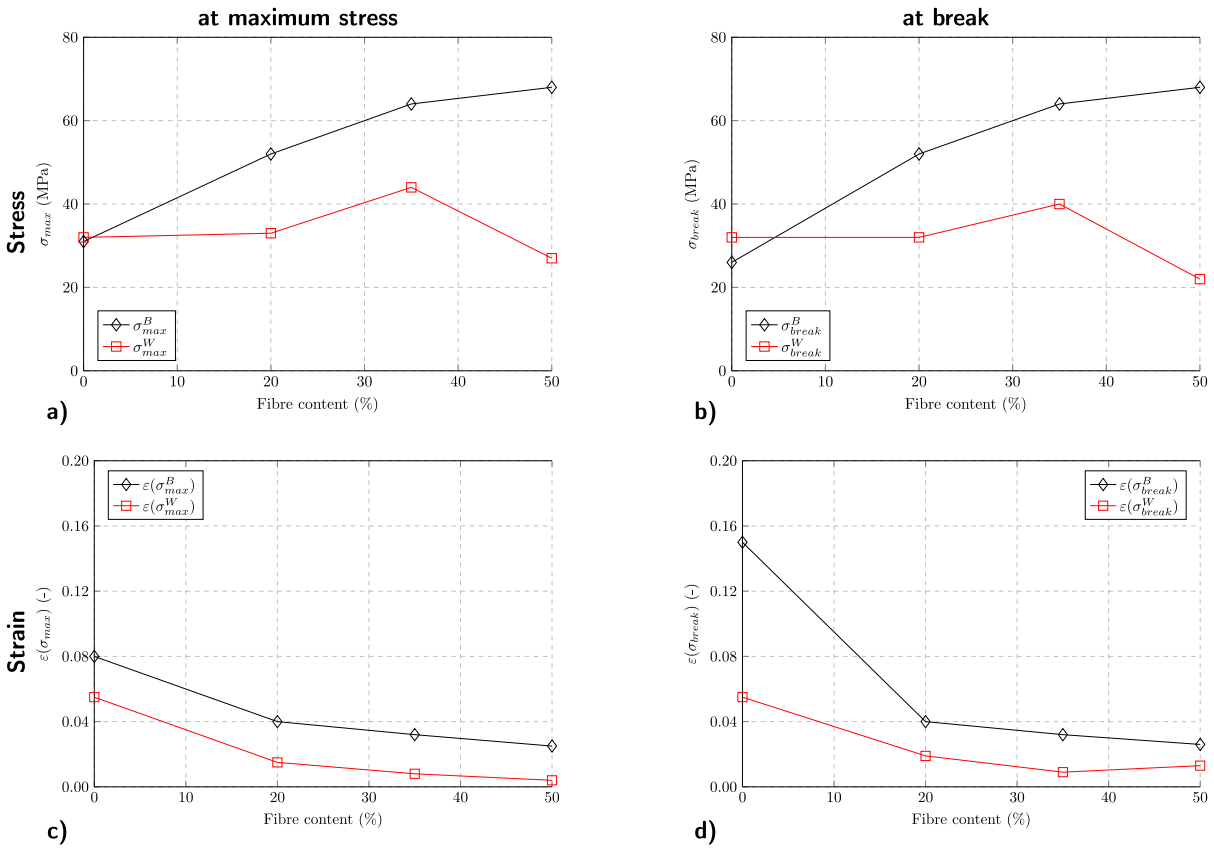

Fig. 15. Evolution of characteristic parameters as a function of the fibre content: (a-b) Stresses; (c-d) Strains. Left column (a, and c) at σ_{max}; Right column (b, and d) at σ_{break}.

Table 4
Characteristic maximum and at break values for base and welded samples.

Composite	Position	σ^B (MPa)	$\varepsilon(\sigma^B)$(-)	σ^W (MPa)	$\varepsilon(\sigma^W)$(-)
PP-GF0	Maximum σ_{max}	31	0.08	32	0.055
	Break σ_{break}	26	0.15	32	0.055
PP-GF20	Maximum σ_{max}	52	0.04	33	0.015
	Break σ_{break}	52	0.04	32	0.019
PP-GF35	Maximum σ_{max}	64	0.032	44	0.008
	Break σ_{break}	64	0.032	40	0.009
PP-GF50	Maximum σ_{max}	68	0.025	27	0.004
	Break σ_{break}	68	0.026	22	0.013

Table 5
Local characteristics for base and weld materials.

Composite	E^B (MPa)	E^W (MPa)	Position	$\varepsilon(\sigma^B)$(-)	$\varepsilon(\sigma^W)$(-)
PP-GF0	1360	880	Maximum σ_{max}	0.06163	0.0957
			Break σ_{break}	0.06163	0.0957
PP-GF20	3950	3750	Maximum σ_{max}	0.01571	0.1164
			Break σ_{break}	0.01571	0.1164
PP-GF35	7100	5000	Maximum σ_{max}	0.00764	0.0365
			Break σ_{break}	0.00855	0.1510
PP-GF50	15 000	4700	Maximum σ_{max}	0.00215	0.0385
			Break σ_{break}	0.00175	0.2537

is available on both base and welded materials. Regardless of the fibre content, welded materials were less deformed than the base ones. A decrease of the strain at the maximum stress as seen in Fig. 15c deals with stiffening of the materials, equivalent to an increase in the Young's moduli.

For Fig. 15d, the two steps decrease of the strain at break could be also observed. The same comments as in Fig. 15c remain valid. But a decrease of the strain at break means embrittlement of the materials.

A cross comparison of Figs. 15c and 15d led to the following notices. The strain at break of the base material of PP-GF0 was the greatest ($\varepsilon(\sigma^B_{break}) \simeq 0.15$ in Fig. 15d) due to the gradual stress softening seen in Fig. 3. Indeed, the strain at the maximum stress $\varepsilon(\sigma^B_{max})$ in Fig. 15c is lower by an order of magnitude than $\varepsilon(\sigma^B_{break})$ in Fig. 15d. For reinforced polypropylene (PP-GF20/35/50), base materials showed the same value of the strain at maximum stress and the strain at break. For welded samples (open diamonds), by opposition, the strain at break (Fig. 15d) is slightly higher than the strain at maximum stress (Fig. 15c).

Appendix B. Local characteristic values for base and weld materials

The apparent local Young's moduli E^B and E^W, respectively for the base and weld materials, are noted in Table 5. Recall that E^B values were the same for both global and local measurements of the engineering strains – with exception of PP-GF50, in which the local E^B was higher than the global one – allowing a focus on the local stress–strain curves in the following. Indeed, as mentioned above, the welded samples are in series so that for the whole specimen the engineering stress is homogeneous. The analysis will then be based on the local strains experienced by the two materials (base and weld) at two specific stress levels of the weld: the maximum stress σ_{max} and the stress at break σ_{break}. The values of the local strains, corresponding to σ_{max} and σ_{break}, were also collected in Table 5 for each fibre content.

Fig. 16 illustrates the data summarised in Table 5. Similar to the structure of Appendix A, the interpretation will be divided in two parts: (i) from Weld-GF0 to Weld-GF20, dedicated to the effect of the reinforcement; (ii) from Weld-20 to Weld-50, dealing with the effect of an increase of the fibre content.

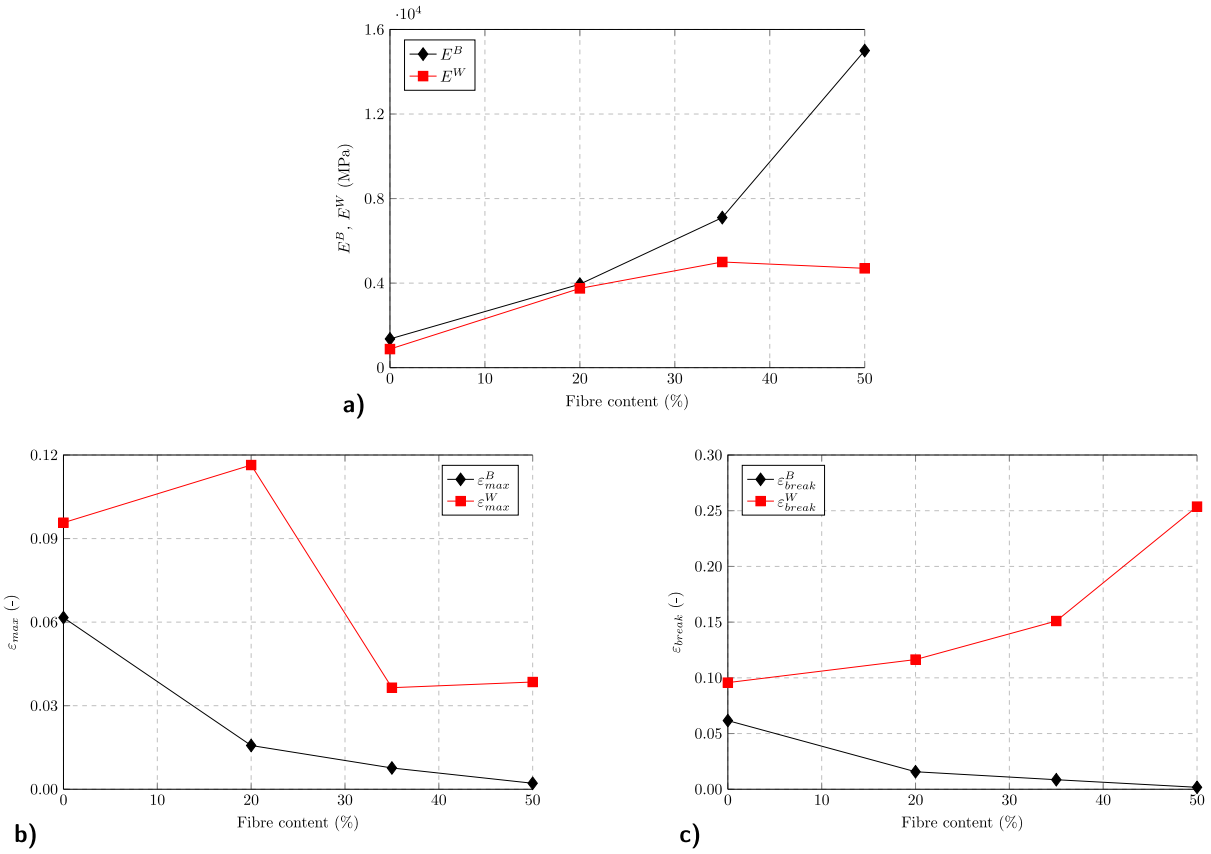

Fig. 16. Evolution of the local characteristic parameters as a function of the fibre content: (a) Young's moduli (E_B, E_W), (b) the strain at the maximum stress ε_{max}, and (c) the strain at break ε_{break} (See Table 5).

Young's moduli

Fig. 16a shows an increase of the Young's moduli for both base (E^B) and weld (E^W) materials when adding 20% of reinforcement. Indeed, adding fillers like short fibres oriented in the longitudinal direction stiffens both materials, at least, up to 20% of fibre content.

Concerning the effect of increasing the fibre content from 20% to 50%, while the base material went on stiffening, the weld one seemed to stabilise in term of stiffening and even exhibited a slight softening (decrease in E^W) from 35% to 50%. A decrease in E^W means that the weld material experiences more deformation than the base material at the same stress level in the linear elastic regime.

Strains at ultimate strength of the weld

The stiffening or softening of the materials should induce respectively a decrease or an increase of the engineering strain, as long as the deformation range is included in the (visco)-elastic part of the stress–strain curve. It is assumed here that this is the case at the ultimate strength (maximum stress) of the weld. To this end, Fig. 16b shows the evolution of the strain corresponding to σ_{max} of the weld.

The effect of adding a reinforcement of 20% in a neat PP consisted of a decrease of $\varepsilon(\sigma_{max})$ (stiffening) for the base material, but a slight increase (softening) of the same strain for the weld. The difference in the trend between the Young's modulus and the strain at σ_{max} is attributed to that the weld exhibited a more significant non linear part in the stress–strain curve. Now, increasing the fibre content from 20% to 50% induced a continuous decrease but at a slower rate of the strain at σ_{max} for the base materials. At the same configuration, the weld showed a significant drop of the strain at ultimate strength from Weld-GF20 to Weld-GF35, followed by a stabilisation of this strain up to Weld-GF50.

Strains at break of the weld

The same analysis as in the previous subsection was carried out, but this time at the important event of the failure of the weld. The engineering stress and strain at break are known. The partition of the strains in each VOI will be discussed, having in mind that the global strain at break, easily accessible experimentally, consists of the sum of twice the local strain in the base material plus the local strain in the weld.

In Fig. 16c, it is shown that adding a reinforcement of 20% in a neat PP resulted in effects similar to that occurring at the ultimate strength of the weld. Indeed, a decrease of $\varepsilon(\sigma_{break})$ (stiffening) for the base material and an increase (softening) of the local strain for the weld can be observed. This time, the deformation measured in the weld integrate the whole stress softening process and the plateau stress which do not appear in the base material. In the next step, consisting of an increase in the fibre content from 20% to 50%, a continuous decrease of the strain at σ_{break} for the base materials together with a continuous increase of the strain at failure of the weld were simultaneously observed. It is to be noted that the strains measured in the base materials were very small: from 0.06 for PP-GF0 to 0.002 for PP-GF50. The strain is then essentially supported by the weld.

The nature of the local strain will be analysed in the next step. To this end, an attempt was made in Fig. 17 to track the evolution of three parameters, as a function of the longitudinal strain $\delta l/l_0$: The transverse strain $\delta w/w_0$, and both the Poisson's ratio ν and the volume change $\Delta V/V_0$, deduced respectively by Eqs. (10) and (11).

Graphs in the left column display F/S_0 in the first Y-axis and $\delta w/w_0$ in the second Y-axis. The right column is dedicated to the Poisson's ratio ν in the first Y-axis and the volume change in the second Y-axis. Only the graphs in the right column have the same scale, allowing a better comparison of the values of the parameters.

For the weld of neat PP-GF0, Fig. 17a shows the continuous increase of the stress–strain curve without any peak stress; together with a continuous decrease but at very small value of the transverse strain (full triangles). Fig. 17b plots the evolution of the Poisson's ratio and

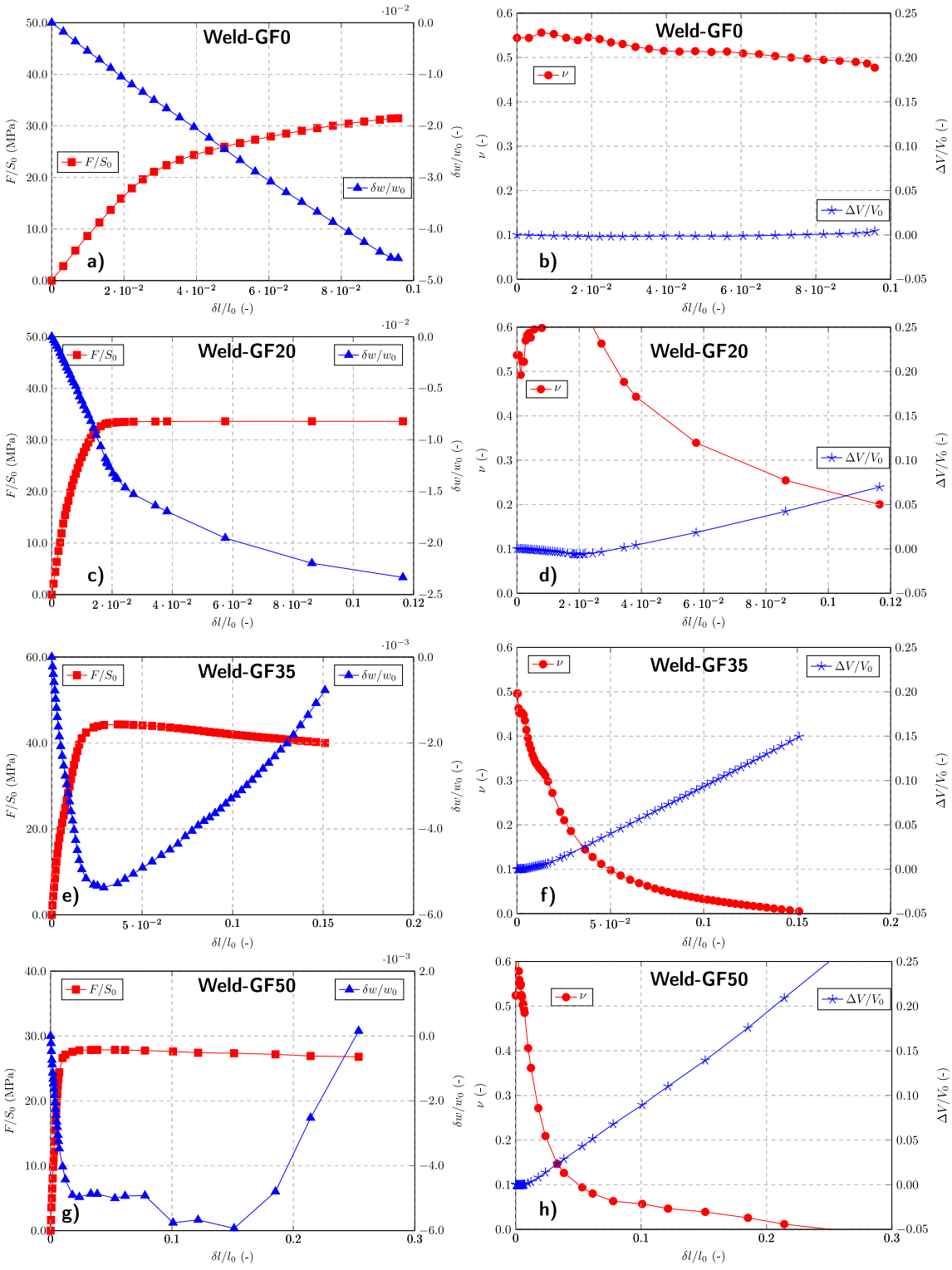

Fig. 17. Evolution of the local contraction $\delta w/w_0$, Poisson's ratio ν, and volume change $\Delta V/V_0$ during deformation at the welded zone for all SGF concentrations. Local stress–strain curve at the welded zone is in full red squares.

the volume change with respect to the local longitudinal strain. Full circles correspond to the Poisson's ratio which values are in most cases higher than 0.5. This is attributed to experimental artefacts due to the small values of the strains and the involved uncertainties. For the whole stress–strain curve, the Poisson's ratio is assumed to be 0.5. Indeed, the corresponding volume change (star symbols) was estimated to be zero. Weld-GF0 can be considered as an incompressible material, from surface measurements.

For Weld-GF20 in Fig. 17c, a "pseudo" yield stress appeared at $\delta l/l_0 \simeq 0.02$ followed by a stress plateau. The transverse strain shows two slopes: steeper before the yield stress and more smooth in the plateau region. In terms of Poisson's ratio, Fig. 17d clearly shows that before the yield stress, $\nu \geq 0.5$. Then, it decreases down to 0.2 at the

failure of the weld. The volume change starts to increase at $\delta l/l_0 \simeq 0.02$ and reaches the small value of 0.07 at the failure of the weld. This type of response is attributed to still Weld-GF0 matrix but perturbed by sparse short fibres.

Significant changes of the trends occurred in Fig. 17e, dealing with Weld-GF35. The stress–strain curve clearly show a peak stress followed by a gradual stress-softening until the failure of the weld. The evolution of the transverse strain shows a decrease up to the peak stress followed by an increase up to the failure. In Fig. 17f, the Poisson's ratio starts at 0.5, decreases down to 0.3 at the peak stress and ends by reaching zero value at the failure of the weld. Accordingly, the volume change can be neglected up to the peak stress but increases quickly in the consecutive stress-softening. The volume change at the failure of the weld was evaluated at 0.15.

Weld-GF50 in Figs. 17g-h exhibited the same characteristics as the Weld-GF35, apart from the volume change at the failure of the weld, which reached a value as high as 0.25.

References

[1] Implementing plastic and polymer composite lightweighting solutions to meet 2025 corporate average fuel economy standards. American Chemistry Council; 2015.

[2] Kagan VA. Joining of nylon based plastic components–Benefits of vibration and hot plate welding technologies. J Inject Molding Technol 2000;4(8).

[3] Węglowski MS. Friction stir processing – State of the art. Arch Civil Mech Eng 2018;18(1):114–29.

[4] Kumar S, Wu C, Padhy G, Ding W. Application of ultrasonic vibrations in welding and metal processing: A status review. J Manuf Process 2017;26:295–322.

[5] Rahmi M, Abbasi M. Friction stir vibration welding process: modified version of friction stir welding process. Int J Adv Manuf Technol 2017;90:141–51.

[6] Zhong Y, Wu C, Padhy G. Effect of ultrasonic vibration on welding load, temperature and material flow in friction stir welding. J Mater Process Technol 2017;239:273–83.

[7] Palardy G, Shi H, Levy A, Le Corre S, Fernandez Villegas I. A study on amplitude transmission in ultrasonic welding of thermoplastic composites. Composites A 2018;113:339–49.

[8] Hamza AA, Jalal SR. A review on manufacturing the polymer composites by friction stir processing. Eur Polym J 2022;178:111495.

[9] Kumar RK, Omkumar M. Experimental investigation on ultrasonic vibration-assisted manufacturing of fiber-reinforced thermoplastics. Mater Manuf Process 2022;37(7):801–8.

[10] Rubino F, Parmar H, Mancia T, Carlone P. Ultrasonic welding of glass reinforced epoxy composites using thermoplastic hybrid interlayers. Compos Struct 2023;314:116980.

[11] Jongbloed B, Teuwen J, Benedictus R, Villegas IF. On differences and similarities between static and continuous ultrasonic welding of thermoplastic composites. Composites B 2020;203:108466.

[12] Stokes VK. Vibration welding of thermoplastics. Part I: Phenomenology of the welding process. Polym Eng Sci 1988;28(11):718–27.

[13] Stokes VK. Vibration welding of thermoplastics. Part II: Analysis of the welding process. Polym Eng Sci 1988;28(11):728–39.

[14] Mofakhami E, Tencé-Girault S, Perrin J, Scheel M, Gervat L, Ovalle C, et al. Microstructure-mechanical properties relationships in vibration welded glass-fiber-reinforced polyamide 66: A high-resolution X-ray microtomography study. Polym Test 2020;85:106454.

[15] Kaushik Pal SF, Panwar V, Gehde M. An investigation on vibration welding of amorphous and semicrystalline polymers. Mater Manuf Process 2016;31(3):372–8.

[16] Lin L, Schlarb AK. Vibration welding of polypropylene-based nanocomposites – The crucial stage for the weld quality. Composites B 2015;68:193–9.

[17] Kagan VA, Roth C. The effects of weld geometry and glass-fiber orientation on the mechanical performance of joints – part I: weld design issues. J Reinf Plast Compos 2004;23(2):167–75.

[18] Kagan VA, Roth C. The effects of weld geometry and glass-fiber-orientation on the mechanical performance of joints - part II: kinetics of glass-fiber-orientation and mechanical performance. J Reinf Plast Compos 2004;23(16):1687–94.

[19] Dai X, Bates P. Mechanical properties of vibration welded short- and long-glass-fiber-reinforced polypropylene. Composites A 2008;39(7):1159–66.

[20] Patham B, Foss PH. Thermoplastic vibration welding: Review of process phenomenology and processing–structure–property interrelationships. Polym Eng Sci 2011;51(1):1–22.

[21] Yuan S, Li S, Zhu J, Tang Y. Additive manufacturing of polymeric composites from material processing to structural design. Composites B 2021;219:108903.

[22] Kamal MR, Chung Y-M, Gomez R. Three-dimensional fiber orientation in vibration welded joints of glass fiber reinforced polyamide-6. Polym Compos 2008;29(9):954–63.

[23] Fiebig I, Schoeppner V. Influence of the initial fiber orientation on the weld strength in welding of glass fiber reinforced thermoplastics. Int J Polymer Sci 2016;2016.

[24] Fiebig I, Schoeppner V. Influence of fiber orientation and weld position in welding injection-molded fiber-reinforced thermoplastics. Welding in the World 2018;62(6):1301–9.

[25] Thomason JL, Nagel U, Yang L, Bryce D. A study of the thermal degradation of glass fibre sizings at composite processing temperatures. Composites A 2019;121:56–63.

[26] Garcea S, Wang Y, Withers P. X-ray computed tomography of polymer composites. Compos Sci Technol 2018;156:305–19.

[27] Reano AF, Guinault A, Richaud E, Fayolle B. Polyethylene loss of ductility during oxidation: Effect of initial molar mass distribution. Polym Degrad Stab 2018;149:78–84.

[28] Blaine RL. Polymer heats of fusion. TA Instruments; Thermal Applications Note.

[29] Weitkamp T, Scheel M, Giorgetta J, Joyet V, Roux VL, Cauchon G, et al. The tomography beamline ANATOMIX at Synchrotron SOLEIL. J Phys Conf Ser 2017;849:012037.

[30] Blanc R, Westenberger P. Comparison of riber orientation analysis methods in Avizo. In: 7th conference on industrial computed tomography. Leuven, Belgium; 2017, p. 255–60.

[31] Advani SG, Tucker CL. The use of tensors to describe and predict fiber orientation in short fiber composites. J Rheol 1987;31(8):751–84.

[32] Proudhon H. Pymicro. 2022, https://github.com/heprom/pymicro.

[33] Ovalle C, Boisot G, Laiarinandrasana L. Effects of stress triaxiality ratio on the heat build-up of polyamide 11 under loading. Mech Mater 2020;145:103375.

[34] Fayolle B, Richaud E, Colin X, Verdu J. Review: degradation-induced embrittlement in semi-crystalline polymers having their amorphous phase in rubbery state. J Mater Sci 2008;43(22):6999–7012.

[35] Castelein G. Etude par AFM de la morphologie de surface de polymères semi-cristallins déformés : le PP isotactique [Ph.D. thesis], Lille: Université des Sciences et Technologies; 1996.

[36] Vite M. Relations entre microstructure, propriétés mécaniques et résistance à la rayure du polypropylène injecté [Ph.D. thesis], Université de Savoie; 2009.

[37] Laiarinandrasana L, Jean A, Jeulin D, Forest S. Modelling the effects of various contents of fillers on the relaxation rate of elastomers. Mater Des 2012;33:75–82.

[38] Dorfmann A, Fuller K, Ogden R. Shear, compressive and dilatational response of rubberlike solids subject to cavitation damage. Int J Solids Struct 2002;39(7):1845–61.

[39] Schlarb AK, Ehrenstein GW. The impact strength of butt welded vibration welds related to microstructure and welding history. Polym Eng Sci 1989;29(23):1677–82.

[40] Ognedal AS, Clausen AH, Dahlen A, Hopperstad OS. Behavior of PVC and HDPE under highly triaxial stress states: An experimental and numerical study. Mech Mater 2014;72:94–108.

[41] Olufsen SN, Tekseth KR, Breiby DW, Clausen AH, Hopperstad OS. A technique for in situ X-ray computed tomography of deformation-induced cavitation in thermoplastics. Polym Test 2020;91:106834.

[42] Rolland H, Saintier N, Robert G. Damage mechanisms in short glass fibre reinforced thermoplastic during in situ microtomography tensile tests. Composites B 2016;90:365–77.